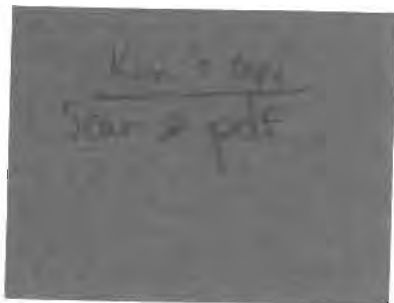


Reprint from

Materials Science and Technology

A Comprehensive Treatment

Edited by R. W. Cahn, P. Haasen and E. J. Kramer



Chapter 7

Zirconium Alloys in Nuclear Applications

by C. Lemaignan and A. T. Motta

from Volume 10 B

Nuclear Materials, Part 2

edited by B. R. T. Frost

Published by
VCH Verlagsgesellschaft mbH
P. O. Box 101161, D-69451 Weinheim
Federal Republic of Germany





7 Zirconium Alloys in Nuclear Applications

Clément Lemaignan

CEA/Centre d'Etudes Nucleaires de Grenoble/DTP/SECC, Grenoble, France

Arthur T. Motta

Nuclear Engineering Department, The Pennsylvania State University,
University Park, PA, U.S.A.

List of Symbols and Abbreviations	2
7.1 History	4
7.1.1 High Temperature Water Reactors	4
7.1.2 Current Use	4
7.2 Fabrication and Products	5
7.2.1 Processing	5
7.2.2 Microstructure	7
7.2.2.1 Alloys and Alloying Elements	10
7.2.2.2 Heat Treatments and Resultant Microstructure	17
7.2.3 Properties	18
7.2.3.1 Mechanical Properties	18
7.2.3.2 Diffusion Data	22
7.3 In-Reactor Behavior	24
7.3.1 Irradiation Damage and Irradiation Effects	24
7.3.1.1 Displacement Calculations	24
7.3.1.2 Irradiation Effects in the Zr Matrix	25
7.3.1.3 Irradiation Effects on Second Phases	28
7.3.1.4 Irradiation Growth	29
7.3.1.5 Irradiation Creep	32
7.3.1.6 Changes in Mechanical Behavior	33
7.3.1.7 Charged-Particle Irradiation	34
7.3.2 Corrosion Behavior	36
7.3.2.1 General Corrosion Behavior	36
7.3.2.2 Oxidation of the Precipitates	37
7.3.2.3 Water Radiolysis	39
7.3.2.4 Hydrogen Pickup	40
7.3.3 Pellet–Cladding Interaction	41
7.4 Challenges	46
7.5 Acknowledgements	47
7.6 References	47

List of Symbols and Abbreviations

a, c	directions $10\bar{1}0$ and 0001 , respectively
a_0, c_0	lattice parameters
A	constant
$\langle a \rangle, \langle c \rangle$	unit cell vectors parallel and perpendicular to the basal plane of Zr
d	oxide layer thickness
D	diffusion coefficient
D_{\parallel}, D_{\perp}	diffusion coefficient parallel, perpendicular to the c -axis
E	energy
E_d	displacement energy
E_s	position of the most stable interstitial
F_x	resolved fraction of basal planes in the direction x
h^{Di}	diffusion enthalpy
K_{Ic}	fracture toughness
K_{ISCC}	SCC stress intensity factor
m, n	exponents
Q	activation energy
ϱ	ratio of thickness reduction to diameter reduction
R	gas constant
t	time
T	absolute temperature
ε	strain
$\dot{\varepsilon}$	strain rate
$\dot{\varepsilon}_x$	strain rate in direction x
$\nu(E)$	number of displaced atoms in a cascade
σ	stress
Φ	neutron flux
AECL	Atomic Energy of Canada Ltd.
ASTM	American Society for Testing Materials
b.c.c.	body-centered cubic
b.c.t.	body-centered tetragonal
BU	burn-up
BWR	boiling water reactor
CANDU	Canadian deuterium uranium reactor
CAP	cumulative annealing parameter ($\sum A$)
CRNL	Chalk River National Laboratory
DAD	diffusion anisotropy difference
DHC	delayed hydride cracking
dpa	displacements per atom
f.c.c.	face-centered cubic
h.c.p.	hexagonal close-packed
HVEM	high voltage electron microscope
IAEA	International Atomic Energy Agency

IGSCC	iodine intergranular stress corrosion cracking
I-SCC	iodine stress corrosion cracking
LHGR	linear heat generation rate
LWR	light water reactor
MIBK	methyl-isobutyl-ketone (process)
PCI	pellet-cladding interaction
PKA	primary knock-on atom
ppm	part per million
PWR	pressurized water reactor
RBMK	Russian graphite-moderated boiling water reactor
RX	fully recrystallized
R&D	research and development
SCC	stress corrosion cracking
SEM	scanning electron microscope
SIPA	stress induced preferential absorption
STEM	scanning transmission electron microscope
SOCAP	second order cumulative annealing parameter
R	stress relieved
TBS	to be specified
TEM	transmission electron microscopy
Trex	tube-reduced extrusion
UTS	ultimate tensile strength
VVER	Voda-Voda energy reactor, Russian type PWR
YS	yield strength

7.1 History

7.1.1 High Temperature Water Reactors

Soon after the observation of the fission of uranium 235, L. Szilard and F. Joliot-Curie recognized the possibility of using the chain reaction phenomenon as a source of energy. Initially, test reactors were designed with no constraints on thermal efficiency. The aim was then to understand neutron physics and to study the behavior of materials under irradiation. Low temperature, pool type reactors were constructed in which the structural material used was exposed to a comparatively mild environment. Aluminum and beryllium alloys were used for core components, due to their low thermal neutron capture cross section and acceptable corrosion rate in water below 100 °C.

Once nuclear power reactors for submarine propulsion and production of electricity were designed, thermal efficiency became mandatory, and materials had to be found that could withstand the high temperature of the coolant, usually water. Zirconium (Zr), with its very low thermal neutron capture cross section, was a potential candidate, but had poor ductility and corrosion resistance. The first pressurized water reactors were loaded with fuel claddings and other structural elements (guide tubes and grids) made of stainless steel.

An improvement in neutron efficiency was a driving force for the development of industrial type Zr-based alloys. At the end of World War II, the nuclear submarine program undertook a large effort in that field. Systematic testing and research and development (R & D) by the U.S. Navy resulted in the development of an efficient hafnium (Hf) separation process and industrial scale ingot production procedures. During the test of a series of binary and

ternary alloys, an accidental contamination of a Zr-2.5% Sn (Zircaloy-1) melt by stainless steel caused the serendipitous discovery of an alloy of good corrosion behavior. Composition variations around this alloy led to Zircaloy-2. Zircaloy-3, a very low tin variant, was soon abandoned in favor of the better Zircaloy-4, a Ni-free variant designed to decrease hydrogen pickup. Similar tinkering with compositional variations to improve corrosion resistance and strength led to the development by the Soviet Union of another family of alloys using the Zr-Nb binary system, later used by Canada as well. The Zr-Nb system allowed the possibility of obtaining a fine two-phase structure that leads to higher strength.

The subject of Zr metallurgy has merited books (Lustman and Kerze, 1955) and reviews (Douglass, 1971; Cheadle, 1975) in the past. Detailed aspects of the metallurgy of the IV-A series (Ti, Hf, and Zr) can be found in Vol. 8, Chap. 8, of this Series. It is the purpose of this work to review the use of Zr for nuclear applications and to present some of the more recent developments in the field.

7.1.2 Current Use

In today's nuclear power reactors, Zr alloys are commonly used for structural components and fuel cladding. For light water reactors (LWR), the common choices are Zircaloy-4 in pressurized water reactors (PWR) and Zircaloy-2 in boiling water reactors (BWR). The heavy water-moderated natural uranium CANDU reactor (Canadian deuterium uranium), as well as the Russian RBMK reactor, use Zr-Nb alloys.

In fuel assemblies and bundles, clad dings are made out of Zircaloy-2 or Zircaloy-4. Those components are exposed to the fission products at the inner surface

at temperatures close to 400°C. At the outer surface they are in contact with light or heavy water at coolant temperatures (from 280 to 350°C). Typical heat fluxes across the cladding are in the range of 30–50 W · cm⁻². Those tubes have different geometries, depending on reactor design (Fig. 7-1). In PWR's fuel rods claddings are 4 to 5 meters long and have a diameter of 9 to 12 mm for a thickness of 0.6 to 0.8 mm. BWR fuel rods are usually slightly larger. In CANDU, fuel bundles are short – 0.5 m – to allow on-line refuelling. The cladding is very thin – 0.4 mm – and is designed to collapse around the UO₂ pellets early during irradiation. In the Russian VVER's the fuel rod geometry is similar to PWR's but the usual cladding alloy is Zr-1% Nb.

Structural components of the fuel assemblies are guide tubes and grids that compose the skeleton. They have to withstand mechanical stresses during normal or accidental operation as well as the oxidizing hot water. In BWR's each assembly is surrounded by a Zircaloy-2 channel box that avoids cross-flow instabilities of the two-phase coolant. Geometrical stability of those components is a critical aspect of core design as it affects fuel loading capability, cooling efficiency and neutron physics behavior of the core.

In the case of CANDU's and RBMK's, the coolant is separated from the moderator and flows around the fuel bundles in pressure tubes, usually made of Zr-Nb alloys. Those large components (10 m × 20 cm × 5 mm) are considered as a structural part of the reactor with a design life of tens of years. They are thus exposed to a high irradiation fluence (up to 3 × 10²⁶ n m⁻²) in contact with the coolant on the inner surface. Mechanical stability of those large components affects the overall geometry of the reactor.

7.2 Fabrication and Products

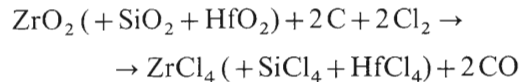
7.2.1 Processing

Zirconium is commonly found in nature associated with its lower row counterpart in Mendeleev's table, hafnium. Most of the common Zr ores contain between 1.5 and 2.5% Hf. Due to its high thermal neutron capture cross section, Hf needs to be removed from Zr for nuclear applications.

The most frequently used ore is zircon (ZrSiO₄) with a worldwide production of about one million metric tons per year. Most of the zircon is used in its original form or in the form of zirconia (ZrO₂) as foundry die sands, abrasive materials or high temperature ceramics. Only 5% is processed into Zr metal and alloys.

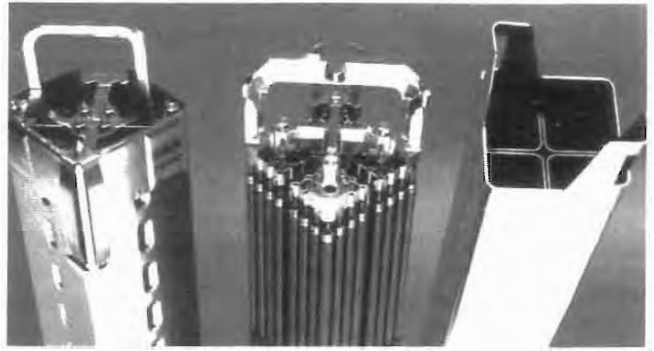
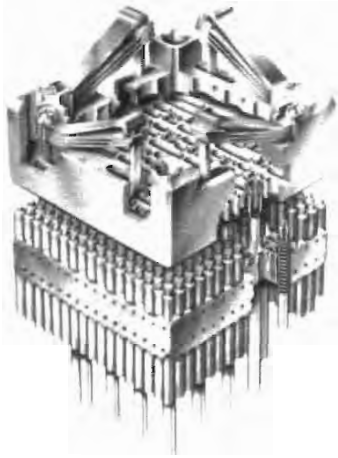
The processing of Zr alloy industrial components is rather complex due to the reactivity of the metal with oxygen. The general scheme is presented in Fig. 7-2: Ore processing, zirconium/hafnium separation, reduction to metal, alloy melting, hot and cold deformation processing.

The first step is to convert the zircon into ZrCl₄, though a carbo-chlorination process performed in a fluidized bed furnace at 1200°C. The reaction scheme is the following:

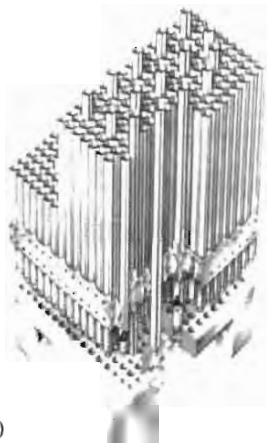
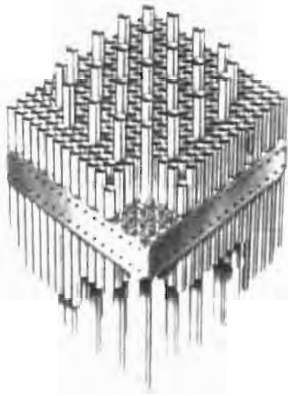


After this step, Zr and Hf are separated using one of the two following processes:

(i) Wet chemical: after reaction with ammonium thiocyanate (SCN NH₄) a solution of hafnyl-zirconyl-thiocyanate (Zr/Hf)O(SCN)₂ is obtained. A liquid-liquid extraction is performed with methyl-isobutyl-ketone (MIBK, name of the process). Hf-free ZrO₂ is obtained after several other chemical steps: hydrochlorination, sulfation, neutralization with NH₃,



(b)



(a)



(c)

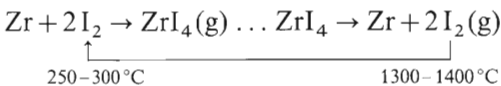
Figure 7-1. Fuel cladding and other components, made of Zr alloys, used in different reactor types: (a) PWR fuel assembly (courtesy FRAGEMA), (b) BWR fuel assembly and channel (courtesy GEC), (c) CANDU fuel assembly and surrounding pressure tube.

and calcination. $ZrCl_4$ is the final result of a second carbo-chlorination process (Stephen, 1984).

(ii) Direct separation process: this is an extractive distillation within a mixture of $KCl-AlCl_3$ as solvent at $350^\circ C$. The vapor phase, generated by a boiler at the lower part of the distillation column, is enriched in Hf, while the liquid phase traps the Zr (Moulin et al., 1984b).

In either case, Zr metal is obtained by a reduction of $ZrCl_4$ in gaseous form by liquid magnesium, at about $850^\circ C$ in an oxygen-free environment. Residual quantities of Mg and $MgCl_4$ are removed from the "sponge cake" by distillation at $1000^\circ C$. After mechanical fracturing, the pieces of sponge are sorted, giving the basic product for alloy ingot preparation.

High purity Zr can be obtained by the Van Arkel process. This consists of the reaction of Zr with iodine at moderate temperature, gaseous phase transport as ZrI_4 and decomposition of the iodide at high temperature on an electrically heated filament, the iodine released being used for the low temperature reaction in a closed loop transport process, according to the following scheme:



For industrial alloys, a compact of sponge containing the alloying elements – O (in the form of ZrO_2), Sn, Fe, Cr, Ni, and Nb – in the desired composition, is melted in a consumable electrode vacuum furnace, usually three times. These vacuum meltings reduce the gas content and increase the homogeneity of the ingot. Typical ingot diameters range between 50 and 80 cm, for a mass of 3 to 8 metric tons.

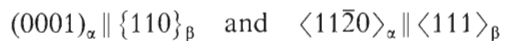
Industrial use of Zr alloys requires either tube- or plate-shaped material. The first

step of mechanical processing is forging or hot rolling in the β phase, at a temperature close to $1050^\circ C$. Hot extrusion is used to obtain tube shells or Trex (tube-reduced extrusion), while hot rolling is used for flat products. For Zircalloys, at that stage a β quench is performed to increase the corrosion resistance of the final product. This treatment controls the distribution of second phase particles, if no further processing is performed above $800^\circ C$ (Schemel, 1977). Further reduction in size is obtained by cold rolling either on standard or pilger-rolling mills. Low temperature recrystallization is performed between the various size reduction steps.

7.2.2 Microstructure

Pure *zirconium* crystallizes at ambient temperature as an hexagonal close-packed metal, with a c/a ratio of 1.593 (i.e., a slight compression in the c -direction compared to the ideal ratio of 1.633). Lattice parameters are $a_0 = 0.323$ nm and $c_0 = 0.515$ nm (Douglass, 1971). The thermal expansion coefficients have been measured by Lloyd (1963) on single crystals. The difference in thermal expansion coefficients between the a and c -directions (see Table 7-1) implies that the c/a ratio tends towards the ideal ratio at higher temperatures – i.e., towards a more isotropic behavior.

At $865^\circ C$, Zr undergoes an allotropic transformation from the low temperature h.c.p. α phase to body centered cubic β phase. On cooling, the transformation is either martensitic or bainitic, depending on the cooling rate, with a strong epitaxy of the α platelets on the old β grains according to the scheme proposed by Burgers (1934) :



The melting of pure Zr occurs at $1860^\circ C$, so it can be classified as a weak refractory

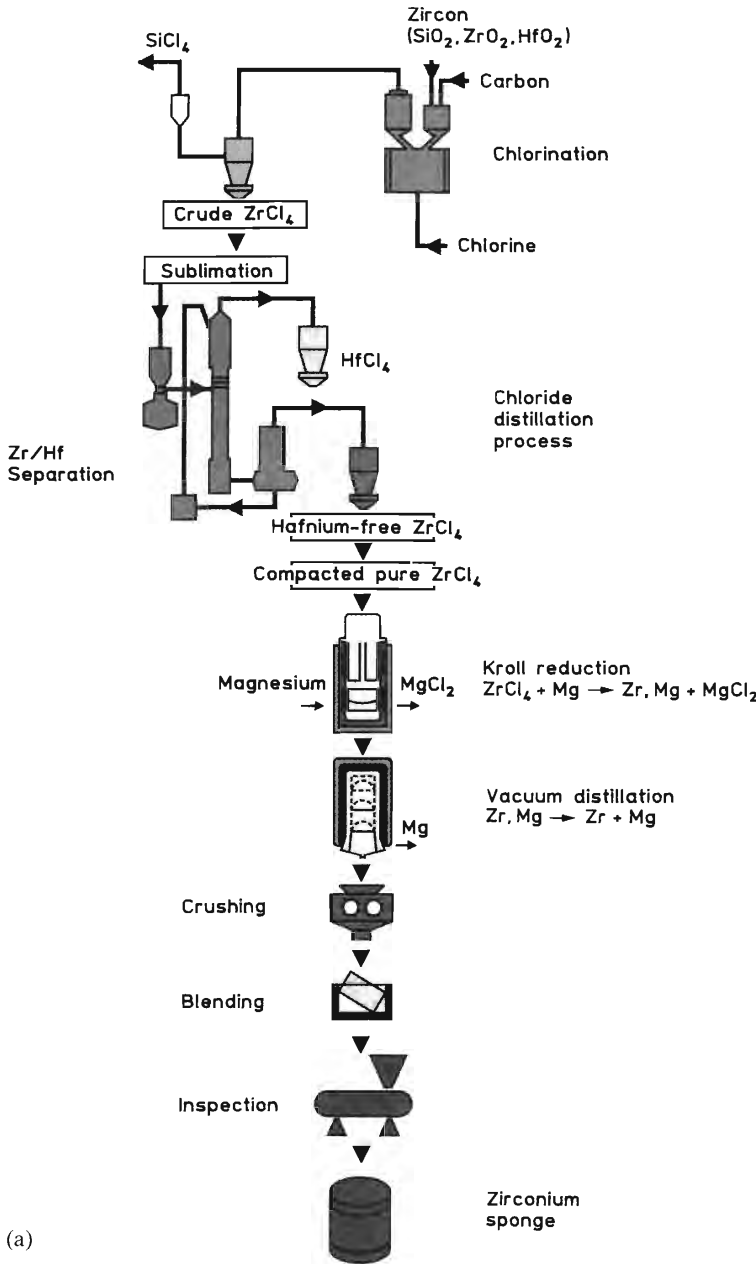
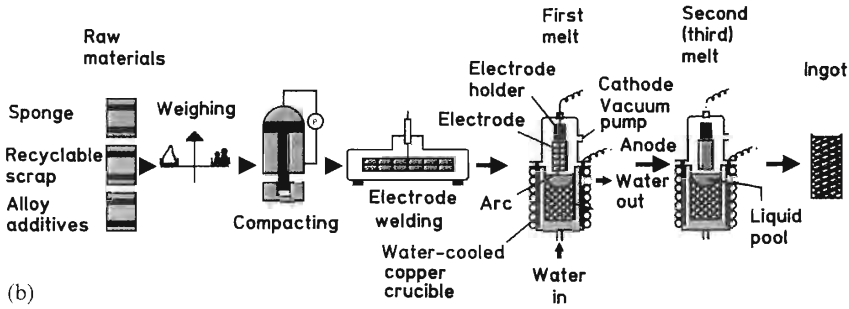


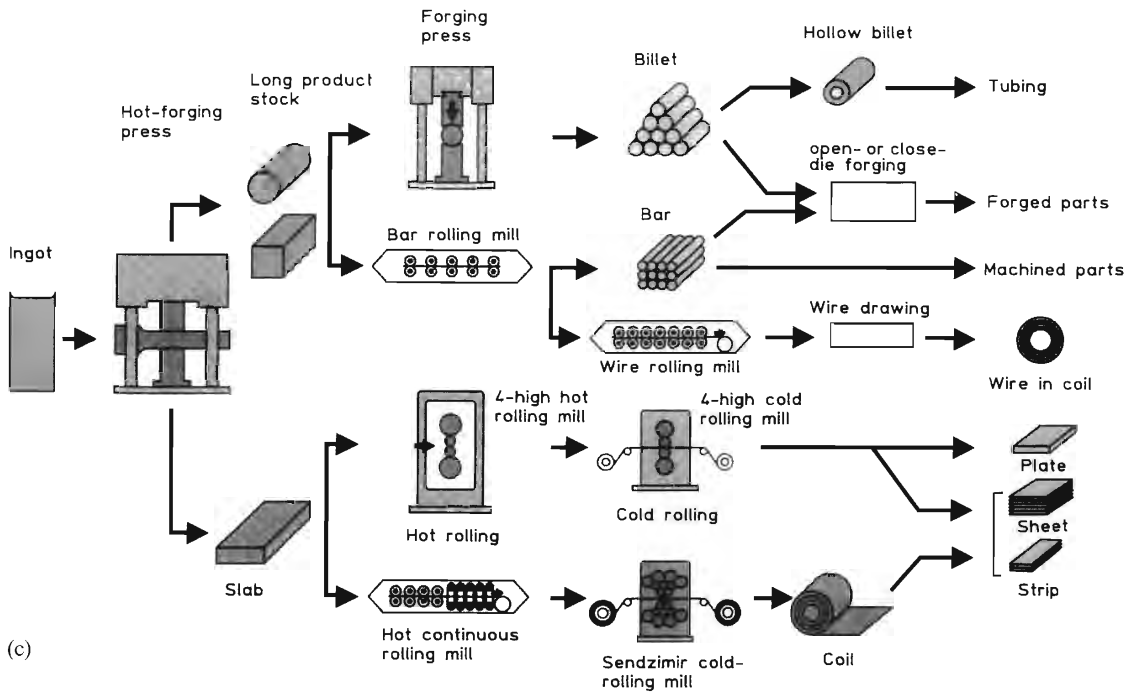
Figure 7-2. Processing and fabrication showing all the steps in the fabrication of Zr alloy components (courtesy CEZUS): (a) From zircon to sponge Zr, (b) from sponge to alloy ingot, (c) from ingot to final product.

metal. The main properties of the Zr and Zr alloys are given in Table 7-1. It should be noticed that the main reason for selecting Zr as a nuclear material is its low thermal neutron capture cross section, which is about 30 times less than that of iron, giving a better thermal reactor neutron efficiency.

One should also note its strong anisotropic behavior. For elastic properties, the differences in thermal expansion and Young’s modulus along the main direction of the hexagonal lattice induce the development of internal stresses after any heat treatment due to grain-to-grain thermal



(b)



(c)

Table 7-1. Major physical properties of Zr.

	Unit	Average	[11 $\bar{2}$ 0] dir.	[0001] dir.
Specific mass	kg · m ⁻³	6500		
Thermal expansion	K ⁻¹	6.70 × 10 ⁻⁶	5.20 × 10 ⁻⁶	1.04 × 10 ⁻⁵
Young's modulus	GPa		99	125
lattice parameter	nm		a ₀ = 0.323	c ₀ = 0.515
Thermal conductivity	W · m ⁻¹ K ⁻¹	22		
Specific heat	J · kg ⁻¹ K ⁻¹	276		
Thermal neutron capture cross section	barn	0.185		

strain incompatibilities; after annealing at 500°C, the $\langle c \rangle$ -planes are thus in tension at stresses up to 85 MPa, depending on the original texture (MacEwen et al., 1983). In a similar way, after plastic strain, elastic recovery is orientation-dependent and leads to compression along the $\langle c \rangle$ planes of almost 200 MPa (Holt and Causey, 1987). For an industrial material, the elastic and thermal expansion coefficients have to be computed from its texture, described either by the pole figures (Rosenbaum and Lewis, 1977) or better by using the complete orientation distribution functions (Sayers, 1987).

The relative solubility of the various alloying elements in the α and β phases is one of the bases for the choice of additions as well as heat treatments.

7.2.2.1 Alloys and Alloying Elements

The zirconium alloys in use today for nuclear applications are limited in number: besides pure Zr, only four alloys are currently listed in the ASTM standards (ASTM, 1990). Those are shown in Table 7-2. The first three are used for cladding and structural materials, like guide tubes in PWRs and BWRs, channel boxes in BWRs and structural materials in CANDU reactors, while the last one, grade R 60904, is used exclusively in pressure tubes for CANDU reactors.

For cladding tubes, only Zircaloy-2 and 4 are listed in ASTM B 811-90. Other alloys have been developed during the history of nuclear power, but except for the Zr-1% Nb alloy used for cladding in Russian PWR's (VVER) (Tricot, 1990), none are in current use anymore, except for specialized applications such as the Zr-Nb-Cu alloy used in garter springs for CANDU pressure tubes.

The needs for better performance of nuclear fuel assemblies and structural parts, mainly with regard to corrosion resistance, has led metallurgists and fuel designers to intensive R & D efforts in order to improve the properties of those Zr alloys by advanced compositions and thermomechanical processing, and to optimize the microstructure within the current ASTM alloy specifications.

Indeed, although safety concerns restrict the introduction of new alloys because of the large amount of data that needs to be accumulated to verify the safe behavior of fuel elements in case of reactor accidents, the specifications for the alloys used today are broad enough for optimization of properties within the specified composition ranges. Moreover, the microstructures may be varied significantly because of the α - β phase transformation of zirconium, and because of the different solubilities of the alloying elements in the different phases. The main alloying elements are now considered in turn:

Oxygen is to be considered as an alloying element, and not an impurity. It is added to the compacts before melting as small additions of ZrO₂ powder. The usual oxygen content is in the range of 800–1600 ppm and its purpose is to increase the yield strength by solution strengthening. A 1000 ppm oxygen addition increases the yield strength by 150 MPa at room temperature, (Armand et al., 1965). Oxygen is an α stabilizer, expanding the α region of the phase diagram by formation of an interstitial solid solution.

The Zr-O phase diagram is given in Fig. 7-3: at high concentration, oxygen stabilizes the α phase to liquid temperatures: During high temperature oxidation, simulating a reactor accident, a layer of oxygen-stabilized α -zirconium is found be-

Table 7-2. Composition range of standard Zr alloys.

ASTM Ref.	R 60802	R 60804	R 60901	R 60904
Common name	Zircaloy-2	Zircaloy-4	Zr-Nb	Zr-Nb
<i>Alloying elements (mass %)</i>				
Sn	1.2 –1.7	1.2 –1.7	—	—
Fe	0.07–0.2	0.18–0.24	—	—
Cr	0.05–0.15	0.07–0.13	—	—
Ni	0.03–0.08	—	—	—
Nb	—	—	2.4 –2.8	2.5–2.8
O	to be specified on order usually 1000–1400 ppm		0.09–0.13	TBS
<i>Impurities (max. ppm)</i>				
Al	75	75	75	75
B	0.5	0.5	0.5	0.5
Cd	0.5	0.5	0.5	0.5
C	270	270	270	150
Cr	—	—	200	100
Co	20	20	20	20
Cu	50	50	50	50
Hf	100	100	100	50
H	25	25	25	25
Fe	—	—	1500	650
Mg	20	20	20	20
Mn	50	50	50	50
Mo	50	50	50	50
Ni	—	70	70	35
Ni	80	80	80	65
Pb	—	—	—	50
Si	120	120	120	120
Sn	—	—	50	100
Ta	—	—	—	100
Ti	50	50	50	50
U	3.5	3.5	3.5	3.5
V	—	—	—	50
W	100	100	100	100

tween the β quenched structure and the zirconia.

Tin is also an α stabilizer. It forms in the α and β phases a substitutional solid solution. Tin-based precipitates have been reported in the literature (Bangaru, 1985) but they appear to be artifacts of TEM sample preparation (Charquet and Alheritière, 1985). At a concentration of 1.2–1.8%, it is used for an increase in corrosion resistance especially by mitigating the deleterious effect of nitrogen in deteriorating

corrosion behavior. Due to a better control of processing parameters, and consequently of nitrogen content, the usage of tin tends to be lower in the current alloys. Tin, however, also has a limited impact on mechanical properties, by increasing the tensile yield strength, and therefore its composition should not be excessively reduced.

Iron, chromium, and nickel are considered as “ β -eutectoids”, because, in their phase diagrams, these elements have an

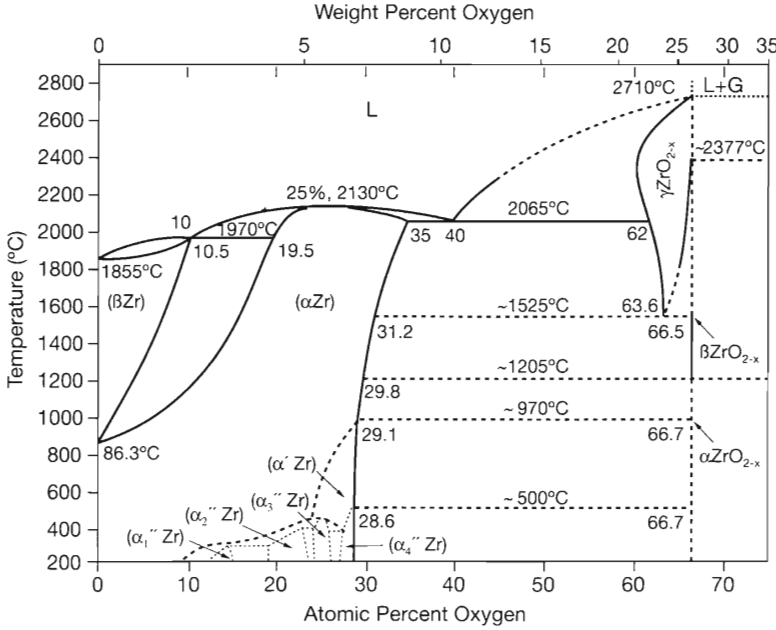


Figure 7-3. Zr-O phase diagram (Abriata et al., 1986).

eutectoid decomposition of the β phase (Fig. 7-4 to 7-6). As mentioned in Sec. 7.1.1, they were added to the early Sn-based alloys after an accidental pollution by stainless steel of a melting lot showed an enhancement in corrosion resistance, leading to the Zircalloys 2 and 4.

At common concentrations, these elements are fully soluble in the β phase. The temperature of dissolution of those elements is in the range of 835–845 °C – that is, in the upper α + β range (Miquet et al., 1982). In the α phase their solubility is very low: in the range of 120 ppm for Fe and

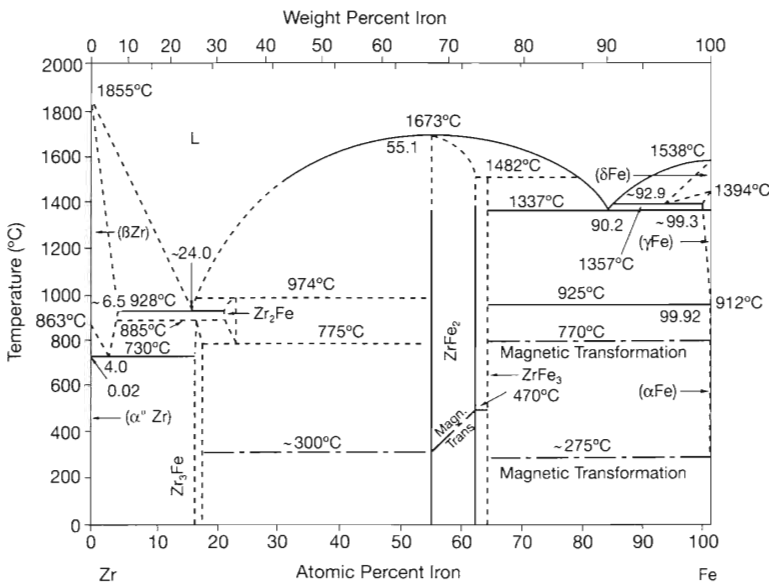


Figure 7-4. Zr-Fe phase diagram (Arias and Abriata, 1988).

$Zr_2(Ni, Fe)$ and $Zr(Cr, Fe)_2$. In Zircaloy-4, the Fe/Cr ratio of those precipitates is the same as the nominal composition of the alloy. In Zircaloy-2 alloys, the partitioning of Fe between the two types of intermetallic phases leads to a more complex relationship between nominal composition and precipitate composition, giving a broad range of Fe/Cr ratio in $Zr(Cr, Fe)_2$, and Fe/Ni in $Zr_2(Fe, Ni)$ (Charquet and Alheritière, 1985; Yang et al., 1986).

The crystal structure of the $Zr(Cr, Fe)_2$ precipitates is f.c.c. (C15) or h.c.p. (C14), depending on composition and heat treatment, with characteristic stacking faults as seen in Fig. 7-7. Both structures are Laves phases. The equilibrium crystallographic structure is dependent upon the Fe/Cr ratio, cubic below 0.1 and above 0.9, and hexagonal in the middle, following an empirical rule proposed by Shaltiel et al. (1976). In common alloys, both types of structures are found, even in the same sample, with random probabilities of occurrences of each. The $Zr_2(Ni, Fe)$ precipitates have a body-centered tetragonal C16 structure (Al_2Cu -type).

The size of these precipitates is of importance for the properties of the alloys, especially the corrosion rate: while better uni-

form corrosion resistance is obtained for Zircaloys used in PWRs if they contain large precipitates, better resistance to localized forms of corrosion is seen in BWRs in materials that have finely distributed small precipitates. It has been shown that precipitation after β quenching is rapid (less than 10 min at 500°C) and that the coarsening rate of those precipitates controls their sizes in the final microstructure. It is thus necessary to consider the complete history of the various heat treatments following the final β quenching to assess the final precipitate size distribution. Various cumulative annealing parameters (CAP or ΣA) have been proposed for this purpose, based on recrystallization activation energy or corrosion behavior. Recently, the coarsening kinetics have been shown to be second order with an activation energy of $Q/R = 18\,700$ K, and a better description of the resultant precipitate size distribution results from using the second order cumulative annealing parameter (SOCAP) (Gros and Wadier, 1989).

In the $Zr-2.5\%Nb$ alloy used in CANDU pressure tubes, very little Fe is found in the α phase, most of it being in the remanent β phase, in metastable solid solution.



Figure 7-7. Typical distribution of second phase precipitates $Zr(Cr, Fe)_2$ and $Zr_2(Ni, Fe)$ in recrystallized Zircaloy.

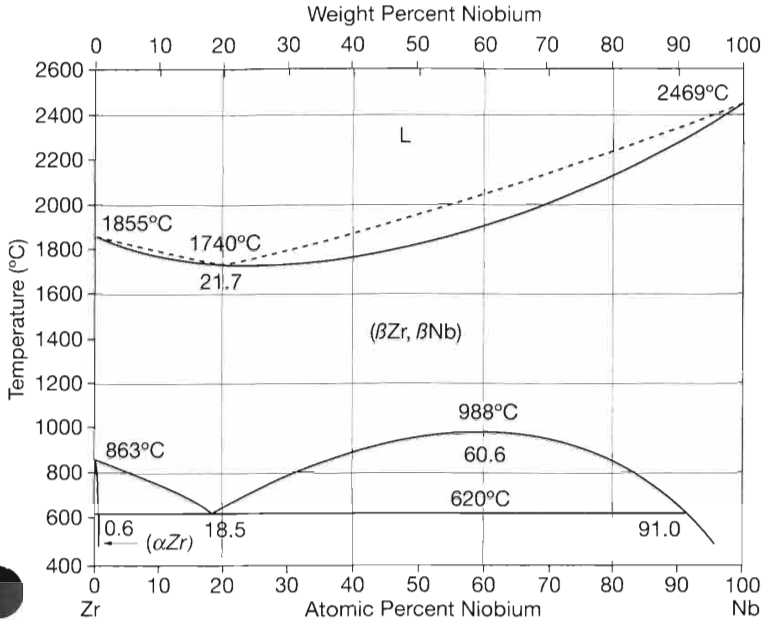


Figure 7-8. Zr-Nb phase diagram (Abriata and Bolcich, 1982).

Niobium (columbium) is a β stabilizer. From pure β -Zr to pure Nb there exists a complete substitutional solid solution at high temperature (Fig. 7-8). A monotectoid transformation occurs at about 620°C and around 18.5 at.% Nb. By water quenching from the β or upper $\alpha + \beta$ regions, the β Nb-rich grains transform by martensitic decomposition into an α' supersaturated h.c.p. phase; subsequent heat treatment below the monotectoid temperature leads to the precipitation of β' Nb precipitates at twin boundaries of α' needles (Williams and Gilbert, 1966). In addition a metastable ω phase can be obtained from the β by slow cooling or aging of a quenched structure. A simple epitaxial relationship is obtained between the ω phase and the parent β (Dawson and Sass, 1970).

Hydrogen is not an alloying element by design, but its behavior has to be assessed, since during waterside corrosion, both the hydrogen produced by the reduction of the water for oxidation of the Zr matrix and

the hydrogen present for water chemistry control, can be absorbed to some extent into the bulk of the alloy. Hydrogen atoms are located at tetrahedral sites of the h.c.p. cell of the Zr matrix up to the solubility limit (about 15 ppm at 200°C and 200 ppm at 400°C). Above the solubility limit hydrogen precipitates as the equilibrium δ f.c.c. phase ($\text{ZrH}_{1.66}$). The corresponding phase diagram is given in Fig. 7-9. High cooling rates cause the precipitation of the metastable body centered tetragonal γ phase, ZrH (Weatherly, 1981).

Due to the volume expansion induced by the precipitation of the hydrides, this new phase tends to reduce its strain energy by nucleating on low index crystallographic planes. Habit planes are $\{10\bar{1}0\}$ for pure Zr and $\{10\bar{1}7\}$ for Zircalloys, in epitaxy with the matrix according to the relationship $(111)_{\delta} \parallel (0001)_{\text{Zr}}$ (Bradbrook et al., 1972). Further macroscopic growth of the hydride clusters occurs in the plane of maximum tensile stresses or in the basal plane if unstressed (Kearns and Woods,

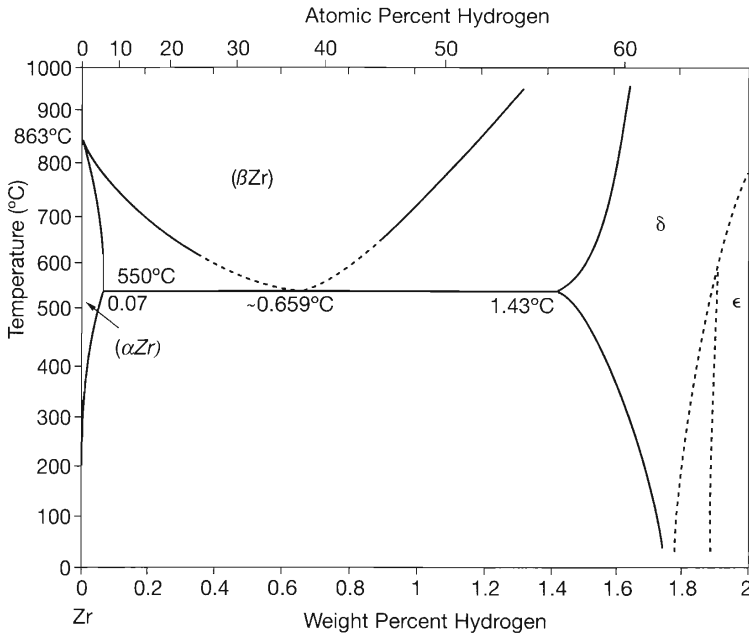
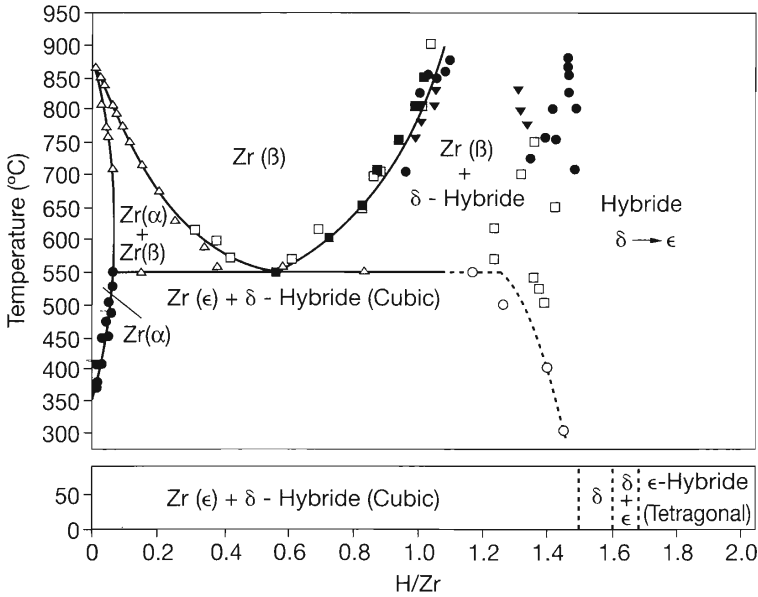


Figure 7-9. Zr-H phase diagram (Zuzek et al., 1990).

1966). Thus the texture of the material as well as the stress state are critical parameters for the control of the precipitation morphology of the hydrides, a brittle constituent at low temperatures.

Other minor constituents are often found in the form of precipitates. Among them are the carbide f.c.c. ZrC and silicides c phosphides of various stoichiometries (Zr₃Si, ZrSi₂, ZrP, Zr₃P) (Charquet and Alheritière, 1985).

7.2.2.2 Heat Treatments and Resultant Microstructure

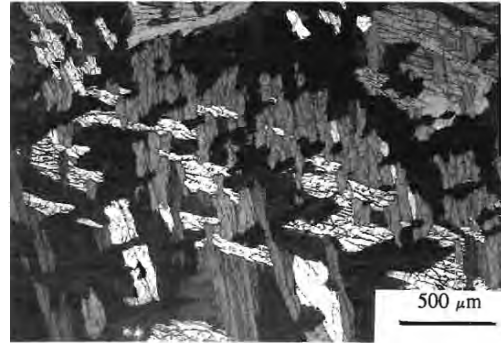
At high temperature, the oxide layer that develops during forging is not protective and therefore O, N, and H can diffuse into the bulk of the ingot if no particular care is taken.

Some of the precautions that have to be taken for thermomechanical processing are reducing the time at high temperature in unprotected atmospheres and performing intermediate descalings and etchings of oxidized forgings.

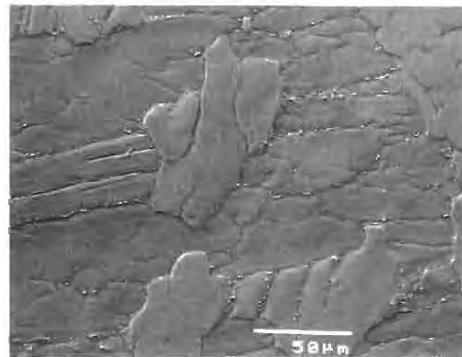
Thus, after ingot melting, the thermomechanical processing commonly used for industrial alloys is the following:

- Hot forging in the β range (1000 to 1050 °C).
- Water quenching from the homogeneous β phase (above 1000 °C).
- Intermediate temperature (upper α) forging and rolling, or extrusion for tubes.
- A series of cold temperature rollings followed by intermediate anneals in vacuum furnaces.

Homogenization in the β phase leads to the complete dissolution of all the second phase particles, but gives rise to significant grain growth: after 30 min at 1050 °C, grain size may reach several millimeters. During the water quench, the β grains transform into α needles by bainitic transformation due to the slow cooling rate of the large pieces involved. These α needles nucleate at grain boundaries and each former β grain leads to a series of crystallographic orientations corresponding to the 12 different permutations of the Burgers relationships. This leads to a typical “basket-weave” microstructure as seen in Fig. 7-10a. The β -eutectoid elements are repelled by the transformation front and precipitate at the boundaries of those



(a)



(b)

Figure 7-10. Typical microstructure of β quench material: (a) Basket weave α grains from the same former β grain. The contrast obtained in polarized light shows the 4 different orientations of the α grains from the same β grain. (b) Second phase precipitation at α grain boundaries. In bright field, the precipitates appear as small white dots at interplate boundaries.

needles (Fig. 7-10 b). This β quench is used for an increase of corrosion resistance of the final product, and is a reference state for further processing. The cold working steps increase the homogeneity of the precipitate distribution.

After each cold working step of plate or tube material, an annealing treatment is mandatory to restore ductility. It is usually performed at 550–600 °C to obtain the fully recrystallized material (RX). The resultant microstructure is an equiaxed geometry of the Zr grains with the precipi-

tates located at the grain boundaries and within the grains (Figs. 7-7 and 7-11).

To improve the mechanical properties of the final product, the temperature of the last annealing treatment can be reduced to avoid complete recrystallization. This is the stress-relieved (SR) state, characterized by elongated grains and a high density of dislocations.

In the case of Zr-2.5% Nb alloys, β quenching in water of small pieces leads to the precipitation of α' martensite supersaturated in Nb. Tempering at intermediate temperature results in β -Nb precipitation at the lath boundaries and at twin boundaries within the lath (Williams and Gilbert, 1966), followed by transformation of α' into α . When quenching is performed from an $\alpha + \beta$ region, a uniform distribution of α and β grains is obtained, and the Nb-rich β phase does not transform. In this later case, however, the texture is less uniform along the length of the tube than in β quenching. After rolling or extrusion, the Nb-rich β grains tend to align and the resultant microstructure is shown in Fig. 7-12. By aging, at temperatures in the range of 500°C, the metastable Nb-rich β phase can be decomposed into an h.c.p. ω

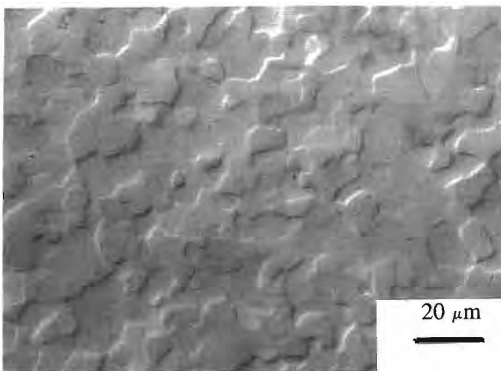


Figure 7-11. Microstructure of recrystallized Zircaloy-4: equiaxed α grains with homogeneous distribution of intermetallic precipitates.

phase. This gives a sharp increase in mechanical strength due to the fine microstructure obtained by the $\beta \rightarrow \omega$ transformation (Cheadle and Aldridge, 1973). In the usual form of the Zr-2.5% Nb, the cold work condition after $\alpha + \beta$ extrusion and air cooling, the microstructure consists of Zr grains with layers of Nb-rich β phase (close to eutectoid composition). Due to the affinity of Fe for the β phase, most of this element is found in the minor β grains. These β grains are metastable and decompose upon aging to a mixture of α -Zr and pure β -Nb. The α -Zr phase itself is metastable and irradiation induced precipitation of the supersaturated Nb solid solution can occur, which is believed to improve corrosion resistance (Urbanic et al., 1989).

In the case of Zr-1% Nb used for VVER and RBMK, the concentration of Nb is low enough to avoid microstructural evolution during service.

7.2.3 Properties

7.2.3.1 Mechanical Properties

The mechanical properties of the Zr alloys are strongly dependent on several parameters such as composition, texture and metallurgical state. For practical purposes, the properties at 300–400°C are most important and room temperature behavior is used mostly for comparison.

As reviewed by Tenckhoff (1988), the deformation mechanism of the hexagonal Zr follows two main mechanisms, slip or twinning, depending on the relative orientation of the grain in the stress field.

Dislocation slip occurs mostly on prism planes in the a -direction. This is referred to as the $\{10\bar{1}0\} \langle 1\bar{2}10 \rangle$ system. The high ductility of the Zr alloys cannot be accounted for solely with this type of slip, which gives only two independent shear

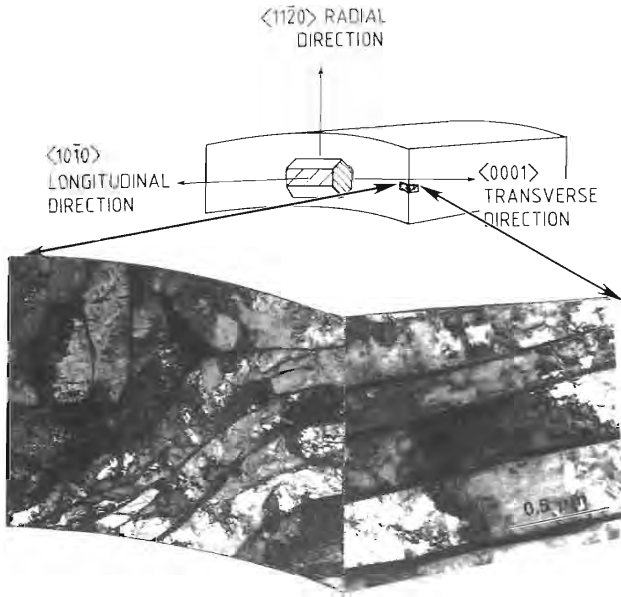


Figure 7-12. Typical microstructure of Zr-2.5% Nb pressure tubes: a layered structure of α Zr and β (Nb-Zr).

systems (by permutation of the indexes). Therefore at high deformations and as the temperature is increased, $(c+a)$ -type slip is activated on $\{11\bar{2}1\}$ or $\{10\bar{1}1\}$ planes.

Twinning. Several systems may be activated depending on the stress state: for tensile stress in the c -direction, $\{10\bar{1}2\}$ $\langle\bar{1}011\rangle$ twins are the most frequent, while the $\{1\bar{1}22\}$ $\langle\bar{1}\bar{1}23\rangle$ system is observed when compression is applied in the c -direction. Twinning is less common in the Zr-Nb alloys than in the Zircaloys because of its fine microstructure.

The resolved shear stresses of the twin systems have been shown to be higher than the one necessary for slip, but due to the dependence of the Schmid factor on orientation, twinning is activated before slip, for some well oriented grains. Therefore there are five independent deformation mechanisms operating in each grain and the von Mises criterion for grain-to-grain strain compatibility is fulfilled.

At the large strains obtained during mechanical processing, steady state interactions occur between the twin and slip sys-

tems that tend to align the basal planes parallel to the direction of the main deformation for rolling and pilgering (Tenckhoff, 1978) and perpendicular to that direction for extruding (Cheadle, 1975). The final texture may change with the specific conditions of the processing mechanisms utilized (Moulin et al., 1984a; MacEwen et al., 1988). The methods of measurement of material texture as well as the impact of texture on the material properties are reviewed in Vol. 15, Chap. 10 of this Series.

For cold-rolled materials (sheets or tubes), the textures are such that the majority of the grains have their c -axis tilted 30–40 degrees away from the normal of the sheet or of the tube surface towards the tangential direction, as can be seen in the $\langle 0002 \rangle$ -pole figure shown in Fig. 7-13. During tube rolling, the spread of the texture can be reduced by changing the ratio of the thickness to diameter reduction (\mathcal{Q} -factor): a reduction in thickness higher than the reduction in diameter gives a more radial texture, i.e., a texture with the c -poles closer to the radial direction.

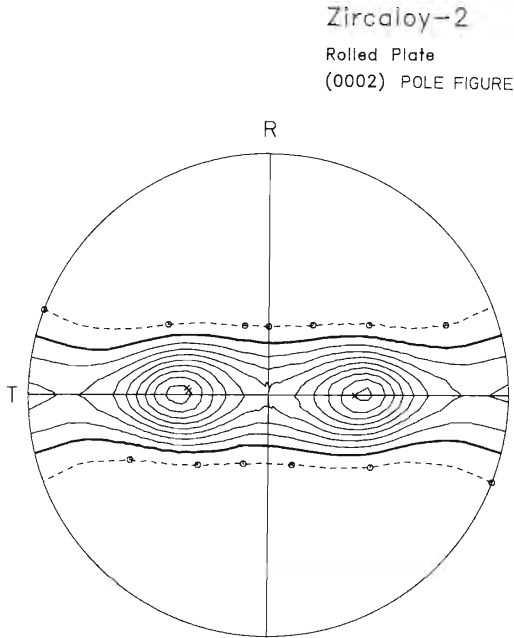


Figure 7-13. Pole figure of 1.5% cold-rolled Zircaloy-2 sheet, showing the distribution of basal planes at 35°C from the normal direction, and along the short transverse direction in the sheet. R indicates the rolling direction and T the short transverse. The normal direction is perpendicular to the page. The thick contour line indicates a random concentration of basal poles, the dotted line is half of random, and each of the thin contour lines indicates an increase of half the random value, so that the maximum corresponds to about five times the random value. (Courtesy of John H. Root, AECL, Chalk River Laboratory.)

After cold processing, the $\langle 1\bar{0}10 \rangle$ -direction is parallel to the rolling direction. During recrystallization heat treatment, a 30 degree rotation occurs around the c -direction and the rolling direction is then aligned with the $\langle 1\bar{1}20 \rangle$ -direction for some of the grains.

At room temperature, in the annealed state, pure, oxygen-free Zr, has a low yield strength of 150 MPa. This yield strength can be enhanced by solution strengthening, using alloying elements that have significant solubilities in α -Zr. Oxygen, tin and niobium are candidate elements to

be considered. Nitrogen would be efficient, but degrades the corrosion resistance. Tin causes only a small increase in tensile strength (Isobe and Matsuo, 1991). By contrast, the addition of 800 ppm of oxygen increases the yield strength to 300 MPa. As a result of this, Zircalloys have minimal yield strengths in the range of 250–300 MPa and the Zr-2.5% Nb alloy, 300 MPa. As in other metals, reduction in grain size is also used to obtain higher strength, leading to the specification of a grain index of 7 or finer for standard products. For all those materials, the ductility remains high (above 20%). Additional strength is obtained by cold working, allowing the increase of the yield strength above 400–450 MPa. This is followed by a final stress-relief heat treatment to restore ductility without drastic reduction in strength.

Finally the texture itself can increase alloy strength by changing the Schmid factor for slip or twinning. This can be observed by the differences in strength between the axial and transverse directions. In addition, due to the distorted shape of the yield locus, and consequently of the orientation of the strain vector, strain is also anisotropic.

The resistance to unstable crack growth (fracture toughness) is relevant to large components under tensile stresses. Therefore, the fracture behavior of the Zr alloys has been studied only in the practical case of the large pressure vessels for chemical engineering (Tricot, 1989) or pressure tubes in CANDU reactors. For hydrogen-free Zr alloys there does not exist any brittle–ductile transition with temperature as in ferritic steels and the rupture is always ductile. The embrittlement of Zr alloys (related to the behavior of hydrogen. During operation, some hydrogen pick-up occurs (see Sec. 7.3.2.4). This hydrogen pre-

precipitates in the form of platelets having a shape which is a function of texture and stress state. It can also diffuse along the thermal gradient, giving locally much higher concentration of hydrides. Those hydrides are not ductile at low temperature, and the fracture behavior of an alloy containing significant amount of hydrogen is strongly dependent on temperature and hydrogen content. The geometrical distribution of the hydrides has also a large influence: in the case of hydrides parallel to the macroscopic plane of the crack, crack growth is enhanced by the percolation of the fractured platelets (Asada et al., 1991). The values reported for the fracture toughness K_{Ic} of different alloys lie in the same range of $120\text{--}150 \text{ MPa} \cdot \text{m}^{1/2}$ for hydrogen free or for high temperature data. The transition temperature is reported around $250\text{--}300^\circ\text{C}$ for 200 ppm of hydrogen and decreases with hydrogen content. For hydrogen content above 400 ppm, the room temperature fracture toughness is reduced below $30 \text{ MPa} \cdot \text{m}^{1/2}$ (Simpson and Chow, 1987; Asada et al., 1991). A reduction of the fracture toughness of Zr-2.5% Nb pressure tubes with the neutron irradiation fluence has been observed and can be linked to the change in microstructure (dislocation density and Nb-rich precipitates).

Thermal creep: The stress applied to structural parts under reactor conditions is sufficient to induce creep. Although in-reactor creep is always mixed with growth (Sec. 7.3.1.4), some experiments were conducted to identify the basic mechanisms of creep strain out-of-flux. Compared with metals of similar melting temperature, the thermal creep rates of zirconium alloys are high and design limitations result from this particular behavior.

Zirconium creeps at low temperature: at room temperature, grain boundary sliding is observed at low strain rates. Early creep

experiments on pure Zr have shown a large variation of the activation energy with temperature, indicating numerous mechanisms involved in this deformation process, that have not been clarified (Guibert et al., 1969). In the range of reactor temperatures, the activation energies of 2.7 eV for standard alloys are close to Zr self diffusion values (see Sec. 7.2.3.2). The stress exponents of the creep rate are still under discussion, reported to be in the range of 2 at high stresses (Matsuo, 1987) or much higher at low stresses (Murty and Adams, 1985). The mechanisms considered are complex with predominance of dislocation glide controlled by local climb.

Due to the texture of the cylindrical components and to the different deformation processes that could be considered, depending of loading path, analytical creep experiments are based on biaxial loading: closed end samples are tested in tension or compression under various internal pressures. Axial and diametral creep strains are measured in order to plot the creep stress locus. Testing stress-relieved (SR) and fully recrystallized (RX) Zircalloys, Murty and Adams (1985) have shown that the results are best explained if prism slip is considered as the active mechanism for RX material and basal slip for SR.

The response of Zr alloys to abrupt changes in loading stress level during creep testing has been discussed in detail and a consensus exists that a strain hardening rule should be used for moderate changes in applied stresses (Lucas and Pelloux, 1981). In the case of large changes of applied stress for reversal loading conditions (tensile/compression) some contribution of recovery has to be considered (Matsuo, 1989).

Most of the metallurgical parameters affect the creep rate. For example, while

Zircaloy-2 and Zircaloy-4 have similar creep strengths for the same thermomechanical processing, Zr-2.5% Nb is much more resistant to creep. The metallurgical state of the material also influences the creep mechanisms: although a SR material has higher tensile strength, its high dislocation density allows it to creep about 2 to 3 times faster than the RX material.

The effect of alloying elements on creep properties has been found to be slightly different from their effect on tensile strength. The effect of oxygen remains important to improve creep resistance, but it is smaller than the room temperature yield strength improvement. Although it has little effect on tensile strength, tin increases the creep resistance (McInteer et al., 1989). Carbon also reduces the creep rate, but due to its low solubility (150 ppm) it cannot be used efficiently for that purpose. Irradiation creep is treated in Sec. 7.3.1.5.

7.2.3.2 Diffusion Data

The large amount of data currently available on solute and self diffusion in α -Zr was reviewed by Hood (1988). In general terms, single crystal, pure materials should be used for the measurements so that there is some confidence that the results represent intrinsic diffusion data. For a review of diffusion in solids see Vol. 5, Chap. 2 of this Series.

The three main considerations in a study of diffusion in α -Zr and α -Zr-based alloys are: the atomic size effect, the anisotropy of diffusion in the hexagonal lattice and the effect of impurities.

Atom size: small solute atoms can diffuse through the interstitial sublattice at rates which may be 10 to 20 orders of magnitude faster than self or substitutional diffusion. Figure 7-14a (Hood, 1988) shows a summary of measurements of intrinsic dif-

fusion in α -Zr (generally extrapolated from high temperatures), and made in single crystal specimens. The fast diffusing small solutes (H, Fe, Ni, up to O and N) are characterized by activation energies between 0.6 and 2.5 eV and pre-exponential factors of the order of 10^{-7} to $10^{-4} \text{ m}^2 \cdot \text{s}^{-1}$. Those elements are thought to be interstitial diffusers. Diffusion of the larger solutes (Zr, Hf, Nb, Sn) has the characteristics of self- or substitutional diffusion, with activation energies of 2.8 to 3.3 eV and preexponential factors of the order of $10^{-4} \text{ m}^2 \cdot \text{s}^{-1}$. The best estimate for the activation energy of Zr self diffusion is 3.3 eV, of which 1.9 eV is the vacancy formation energy and 1.4 eV is the migration energy (Hood et al., 1992). When there is no experimental data, a rough estimate of the migration energy and preexponential can be obtained from the size correlation curves shown in Fig. 7-14b.

Anisotropy: It has been recognized that diffusion along the a and c -axes in Zr is generally different. For that reason, in principle, diffusion measurements in α -Zr have to be made in both directions. In practice this can be done more easily for the fast solutes (Fe, Cr, Ni), for which it has been determined that the diffusion coefficients are maximum along the c -direction, by a factor of $D_{\parallel}/D_{\perp}=3$ (D_{\parallel} is the diffusion coefficient parallel to the c -axis and D_{\perp} is perpendicular to the c -axis). For self diffusion the only measurement available (Hood and Schultz, 1974) gives $D_{\parallel}/D_{\perp}=1.3$. The diffusion of other slow diffusers is also nearly isotropic (Zhou, 1992). The determination of such diffusion anisotropies is important: a factor of two in the diffusion anisotropy has been shown (Woo, 1988) to produce significant effects in sink biases and microstructural evolution through the so-called DAD (diffusion

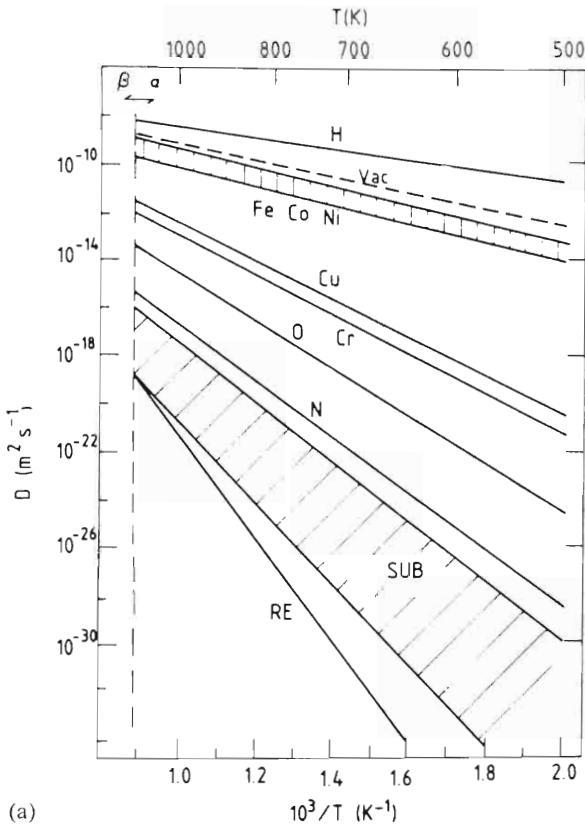
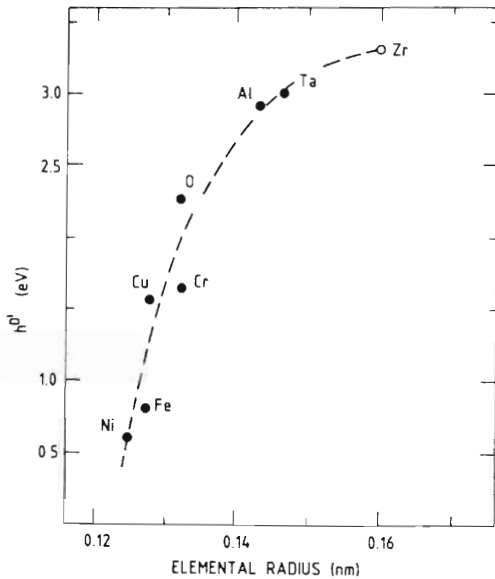
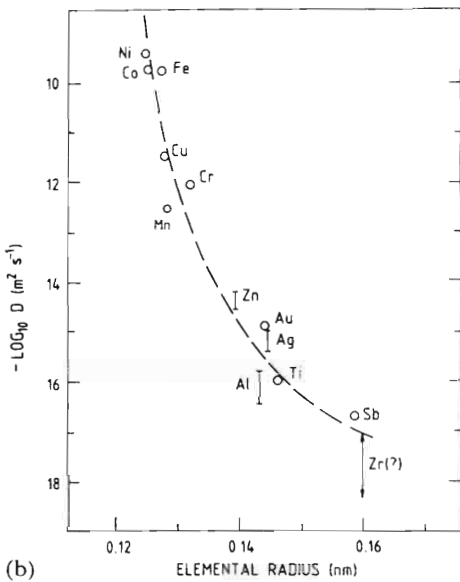


Figure 7-14. (a) Self and solute diffusion data in α -Zr (Hood, 1988). (b) Atom size correlation for migration energy and pre-exponential factor for diffusion in α -Zr (Hood, 1988).



(b)

anisotropy difference) effect, as mentioned in Sec. 7.3.1.4.

Impurities: The effect of impurities on Zr self diffusion has only recently begun to be understood. It was determined that substitutional diffusion in Zr is dominated by the effect of residual Fe. Hf diffusion in nominally pure Zr (~ 50 ppm of Fe) was shown to be higher by up to two orders of magnitude than Hf diffusion in ultrapure Zr (< 1 ppm Fe). In a conclusive experiment, when Fe was added to the ultrapure material, to the levels of the nominally pure material, the Hf diffusion coefficients jumped up to the values observed in the nominally pure Zr (Hood et al., 1992). The Fe-enhanced migration energy is 0.7 eV, in contrast to the intrinsic value of 1.4 eV. It is not known at present what kind of defect configuration and migration mechanism creates such a large diffusion enhancement, e.g., a tightly bound vacancy-Fe complex having been proposed (King et al., 1991).

7.3 In-Reactor Behavior

In this section, we examine the behavior of Zr components when subjected to a nuclear reactor environment.

In Sec. 7.3.1 the effects of the neutron flux in causing irradiation damage to the Zr components are discussed. The effects of this damage range from an increase in the concentration of dislocation loops, causing hardening and loss of ductility and the dimensional changes brought about by irradiation creep and growth, to second phase dissolution, decomposition and re-precipitation, possibly influencing corrosion resistance.

Waterside corrosion of Zr alloys is examined in Sec. 7.3.2. In-reactor, high temperatures, irradiation radiolysis, and, pos-

sibly, deleterious changes in the material combine to accelerate corrosion rates that are normally slow outside irradiation. The effects of alloying elements on corrosion rates are discussed and the special problems of nodular corrosion, and hydrogen/deuterium pickup are considered.

In Sec. 7.3.3, the problem of stress corrosion cracking induced by the pellet-cladding interaction is discussed. This is a typical example of an in-reactor corrosion mechanism, since it requires cladding stresses induced by interaction with the expanding UO_2 pellet, while the corroding agent is iodine originating from nuclear fissions.

7.3.1 Irradiation Damage and Irradiation Effects

7.3.1.1 Displacement Calculations

At the root of all irradiation effects discussed later in this section is the displacement of atoms from their normal lattice positions by collisions with incident particles. In the case of in-reactor behavior, we are concerned with the collisions of neutrons with target atoms.

For the case of zirconium and 1 MeV neutrons, the recoil atom from the original neutron-atom collision (called primary knock-on atom, PKA), has a maximum energy as high as 44 keV. This PKA deposits its energy in a relatively localized region, causing secondary and higher order displacements. The localized nature of the energy deposition creates a region of high displacement density, commonly called a collision cascade. The number of displacements in a collision cascade caused by a PKA of energy E is $\nu(E)$, typical values being about 100 to 200.

The procedure for calculating $\nu(E)$ and relating it to the number of displacements induced in a material by a given neutron

fluence is well explained in the literature (Olander, 1976) and elsewhere in this Volume (Chap. 9, Sec. 9.4.2), so it need not detain us here. In order to perform the calculation, the displacement energy E_d needs to be specified. This is the minimum energy required to displace an atom from its lattice site. According to measurements in the high voltage electron microscope (HVEM) (Griffiths, 1987) E_d for the production of visible damage in pure Zr is about 25 eV, varying by approximately 1 eV with crystallographic orientation. This energy is much higher than the Frenkel pair formation energy, reflecting the fact that the atom has to go through a potential barrier in order to be displaced.

After being displaced from their most stable lattice position, the atoms have a choice of several interstitial configurations to assume, of which the lowest energy ones are more likely to be found. These configurations have been studied by lattice calculations using interatomic potentials that predict macroscopic properties of Zr with some accuracy (Bacon, 1988). The possible defect positions for the h.c.p. lattice are shown in Fig. 7-15. Calculations (Fuse, 1985) show that the most stable interstitial is located at the E_s position, and has an energy of 3.83 eV.

Although the calculation for the conversion of neutron fluence to displacements per atom has to be performed for each specific reactor, with its particular flux characteristics and power history, a reasonable estimate of the conversion factor is 2 displacements per atom (dpa) for each $10^{25} \text{ n} \cdot \text{m}^{-2}$ ($E > 1 \text{ MeV}$). This means that the zirconium rods in a pressurized water reactor (PWR) receive about 20 dpa in the years they stay in the reactor, corresponding to about $10^{-7} \text{ dpa} \cdot \text{s}^{-1}$.

Each atom is therefore displaced on the average about 20 times during the three

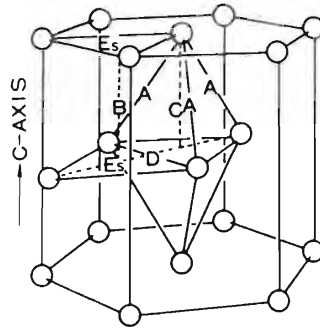


Figure 7-15. Possible interstitial sites for h.c.p. zirconium. Letters in the figure indicate positions and types of interstitials (Fuse, 1985).

years it stays in reactor. Clearly, a lot of annealing takes place concurrently, since the Zr cladding maintains its structural integrity, and most of its good mechanical properties. Some of this annealing takes place within the cascade itself, the number of stable defects produced per displacement being much smaller than 100% (Woo and Singh, 1992). However, the sheer amount of rearrangement that is required creates a potential for microstructural changes under irradiation. The mechanisms by which this potential is translated into actual material changes under irradiation is reviewed in the following sections.

7.3.1.2 Irradiation Effects in the Zr Matrix

Under reactor operating temperatures, the point defects that escape immediate recombination can migrate to sinks, such as grain boundaries, free surfaces and dislocations. Due to the unequal bias of the different sinks for the defects, vacancies and interstitials can accumulate at different sinks, giving rise to macroscopic effects. For example, when network dislocations are not present in large quantities (i.e., in recrystallized material), the point defects can agglomerate into dislocation

loops, causing a large increase in dislocation density.

Dislocation Structure

The as-fabricated material contains network dislocations, resulting from cold work. Those are mixed in type, both $\langle a \rangle$ and $\langle c+a \rangle$ -component dislocations being present.

The dislocation structure in Zr alloys under irradiation was studied in an international "round robin" experiment involving several laboratories (Northwood et al., 1979). The picture was more complete in the review by Griffiths (1988), due to the examination of higher fluence samples. Dislocations developing under irradiation are mostly $\langle a \rangle$ -type $1/3\langle 11\bar{2}0 \rangle$ loops, as shown in Fig. 7-16. Both vacancy and interstitial loops have been reported, in roughly comparable proportions. This is an unusual feature of microstructural development under irradiation in Zr and its alloys, as compared to cubic metals and other h.c.p. metals, where only one type of loop usually grows. Near $\{1\bar{2}12\}$ grain boundaries the $\langle a \rangle$ -type loops are mostly vacancy type, as shown in the denuded zone of Fig. 7-17. The effect is less marked

for grain boundaries parallel to (0001) in which the denuded zones still exist, but are smaller. This indicates that the grain boundaries can be net interstitial sinks.

The $\langle a \rangle$ -type dislocations arrange themselves in layers parallel to the basal plane. Vacancy loops exist at temperatures between 353 and 723 K, above which temperature they are destabilized by vacancy thermal emission, as verified by Jostons, et al. (1979), who measured a decrease in the ratio of vacancy – to interstitial – type loops above that temperature.

After neutron irradiation to around $3 \times 10^{25} \text{ n} \cdot \text{m}^{-2}$ at temperatures between 560 and 773 K, $\langle c \rangle$ -component dislocations start to develop in annealed Zircaloy-2. They are located on the basal plane and are vacancy in character and have a $1/6\langle 20\bar{2}3 \rangle$ Burgers vector. Some of those $\langle c \rangle$ -type loops are shown developing near a dissolving amorphous precipitate particle in Fig. 7-18. It is not known what triggers the appearance of $\langle c \rangle$ -component loops after the aforementioned dose, but they have been linked to the occurrence of breakaway growth by providing an additional sink for vacancies, as explained in Sec. 7.3.1.4. It is interesting to note that under electron irradiation, $\langle c \rangle$ -component

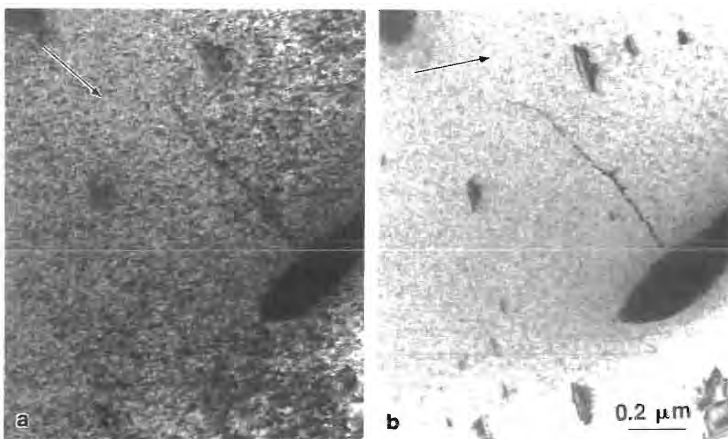


Figure 7-16. $\langle a \rangle$ -type dislocations formed in Zr-2.5 Nb after neutron irradiation at 573 K [(a) diffracting vector $10\bar{1}1$ showing $\langle a \rangle$ -type contrast, (b) diffracting vector 0002 showing $\langle c \rangle$ -type contrast]. No $\langle c \rangle$ -type loops are present (micrograph courtesy of M. Griffiths, AECL, Chalk River).

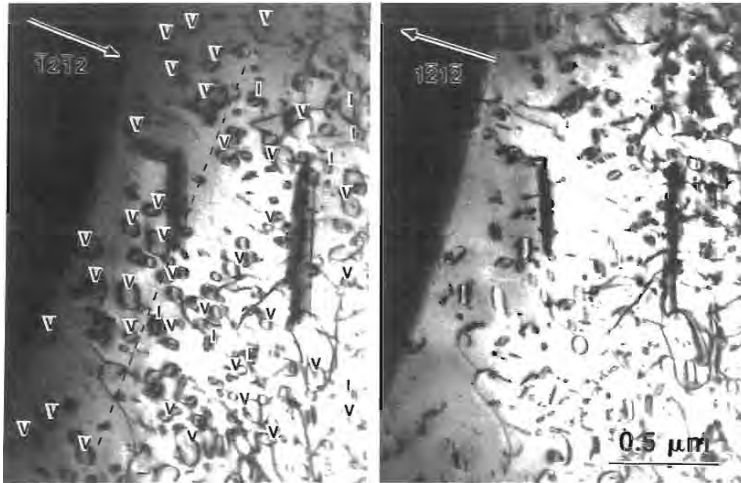


Figure 7-17. Distribution of vacancy and interstitial loops close to a grain boundary in crystal-bar Zr irradiated at 700 K to a fluence of $1.1 \times 10^{25} \text{ n m}^{-2}$ ($E > 1 \text{ MeV}$). Loops exhibiting inside contrast with a 1212 diffraction vector are vacancy in nature (beam direction close to $[1213]$). Close to the grain boundary, vacancy loops form preferentially, in contrast to the bulk, where some interstitial loops also form (micrograph courtesy of M. Griffiths, AECL, Chalk River).

dislocations of the type $1/2[0001]$ and $1/2[11\bar{2}3]$ are found, which supports the general idea of development of $\langle c \rangle$ -type dislocations under irradiation.

Voids

Contrary to the behavior of stainless steel, Zircaloy does not exhibit significant void formation under neutron irradiation (Farrell, 1980). Under electron irradiation swelling is observed in Zr which was previously injected with helium (He) (Faulkner and Woo, 1980). Accordingly, TEM studies have not found many cavities and voids in neutron or charged-particle irradiated Zr alloys. This was confirmed by Baig et al. (1989) who could not find any voids in irradiated Zr by small angle neutron scattering. The reason is thought to be that the gases that could stabilize voids and cavities (O,H,N) are very soluble in the Zr matrix, where their equilibrium concentration can be quite high (Figs. 7-4 and 7-5).

Some cavities have nevertheless been found in crystal bar Zr after neutron irradiation, in the interstitial denuded zone near grain boundaries (Griffiths et al., 1988). This is probably due to the high

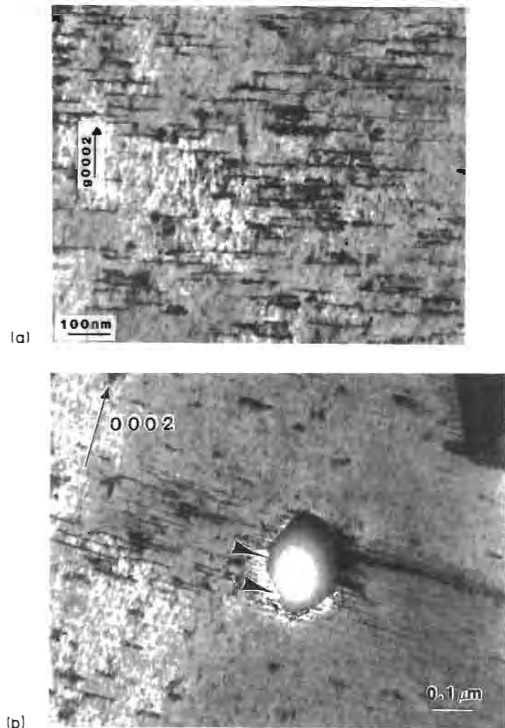


Figure 7-18. (a) Formation of $\langle c \rangle$ -component dislocations in Zircaloy-4 irradiated in a PWR at 580 K to a fluence of $8.5 \times 10^{25} \text{ n m}^{-2}$. Compare with Fig. 7-16b taken under same diffraction conditions. (b) Association of $\langle c \rangle$ -component dislocations with amorphous $\text{Zr}(\text{Cr, Fe})_2$ precipitate, in course of dissolution. Arrows indicate steps similar to those in Fig. 7-19B and C.

vacancy concentration in those regions. For reasons unknown, voids are also found near second phase particles. Their total number density is however quite low and they are not thought to have much effect in the irradiation behavior of zirconium alloys.

7.3.1.3 Irradiation Effects on Second Phases

Crystalline to Amorphous Transformation (Amorphization) of Precipitates

One of the most striking effects of irradiation on Zr alloys is the crystalline to amorphous transformation (amorphization) observed in the intermetallic precipitates $Zr(Cr, Fe)_2$ and $Zr_2(Ni, Fe)$, commonly found in Zircalloys. Those precipitates, described in Sec. 7.2.2, undergo amorphization under neutron irradiation as reported by Gilbert et al. (1985) and confirmed by Yang et al. (1986). The transformation has been observed in Zircalloys irradiated at 550 to 620 K (from both LWR fuel cladding and structural material) and at 350 K (calandria tubes from CANDU reactors). At 350 K, both types of precipitates are completely amorphous after very low fluences (0.5 to 1 dpa). At the higher temperature range, the $Zr_2(Ni, Fe)$ precipitates are completely crystalline, while the $Zr(Cr, Fe)_2$ precipitates are partially amorphous having developed a “duplex” structure, consisting of an amorphous layer that starts at the precipitate-matrix interface, and gradually moves into the precipitate until the precipitate is completely amorphous. This is shown in Fig. 7-19A. A crystalline core is present, as evidenced by the stacking fault contrast, while an amorphous layer has been formed that will eventually envelop the whole precipitate. Amorphization is associated with a depletion of iron from the amorphous

layer into the Zr matrix, while the Cr concentration in the precipitate remains constant.

It is thought amorphization occurs because the irradiated crystalline structure is destabilized with respect to the amorphous phase due to the accumulation of irradiation damage. A review of the experimental evidence and theoretical models for amorphization of those precipitates under neutron and charged particle irradiation was given by Motta et al. (1991) and Motta and Lemaignan (1992).

Precipitate Dissolution and Reprecipitation

After amorphization, precipitate dissolution is accelerated, as illustrated in Figs. 7-19B, C, and D. A serrated interface is formed as the precipitates dissolve, indicating either a dissolution of the precipitate along preferential directions (Yang, 1989), or a minimization of interfacial energy by faceting.

After precipitate dissolution, and post irradiation annealing, Fe and Cr reprecipitate in the matrix, forming Cr-rich precipitates close to the original particle, and iron rich precipitates further away. This illustrates the difference in mobility of those two elements in Zr, mentioned in Sec. 7.2.3.2. It is possible that some of the Fe and Cr remains in solid solution.

Although precipitate dissolution may be accelerated by the amorphous transformation, it also happens under neutron irradiation at higher temperatures, where amorphization does not occur, so amorphization is not a precondition for dissolution.

There have been reports of irradiation induced precipitation and dissolution of other types of precipitates in zirconium alloys. $ZrSnFe$ precipitates have been

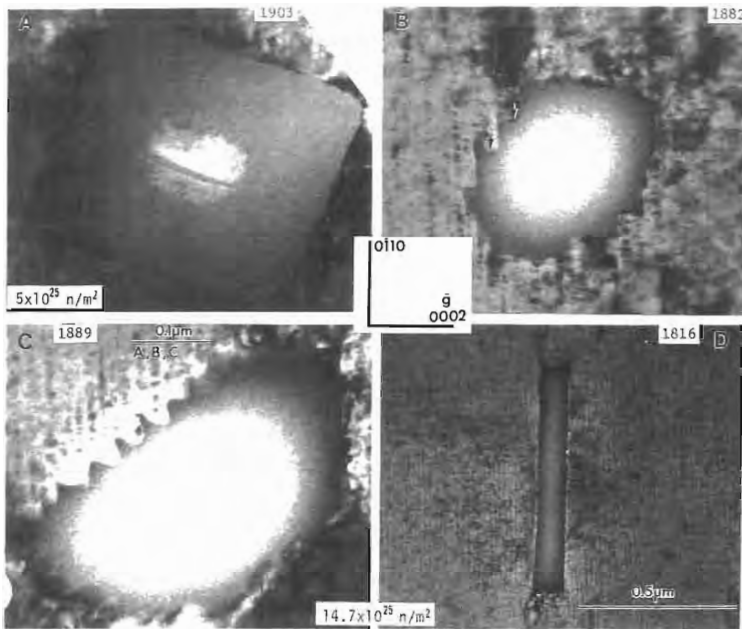


Figure 7-19. Precipitate amorphization and dissolution under neutron irradiation (courtesy of W. J. S. Yang, GE). (A) The duplex structure in a Zr(Cr, Fe)₂ precipitate in Zircaloy-4 irradiated to $5 \times 10^{25} \text{ n} \cdot \text{m}^{-2}$ at 561 K, showing a crystalline core surrounded by an amorphous layer. Iron is depleted in the amorphous layer (B), (C), and (D): Zr(Cr, Fe)₂ precipitate dissolution along preferential crystallographic directions after irradiation to $14.7 \times 10^{25} \text{ n} \cdot \text{m}^{-2}$. The interface facting is arrowed in (B).

found in Excel alloys (Zr-3.5% Sn-1.0% Nb-1.0% Mo) following neutron irradiation to $1.5 \times 10^{26} \text{ n} \cdot \text{m}^{-2}$ at 690 K (Griffiths, 1988). This was paralleled by the observation by Woo and Carpenter (1987) of Zr₅Sn₃ precipitates in Zircaloy-2 following irradiation to $7.4 \times 10^{24} \text{ n} \cdot \text{m}^{-2}$ (>1 MeV) at 875 K (total dose about 3 dpa). These last precipitates were later found to be associated with Fe. Also in Zr-2.5% Nb, the Fe-rich β phase loses its Fe to the α phase, and extensive precipitation of fine-sized Nb rich precipitates in the α phase has been reported as a result (Coleman et al., 1981). This is shown in Fig. 7-20.

Outside irradiation, by contrast, the β phase decomposes under thermal annealing to a mixture of Zr-86% Nb and the intermetallic (Zr, Nb)₃(Fe, Cr).

Second phase redissolution and redistribution of alloying elements, can have important consequences for irradiation growth and corrosion resistance, as explained below and in Sec. 7.3.2.

7.3.1.4 Irradiation Growth

Irradiation growth refers to the dimensional changes at constant volume of an unstressed material under irradiation (Fidleris, 1988). For Zr single crystals, irradiation growth consists of an expansion along the *a*-direction, and corresponding contraction along the *c*-axis.

In polycrystalline materials the situation is more complex, since grain boundaries can act as biased sinks for point defects, so that grain shape and orientation play a large role. Usually, however, growth behavior of polycrystalline materials also consists, of expansion along the *a*-direction and contraction along the *c*-axis. As noted in Sec. 7.2.3.3, the fabrication process of Zr alloy components induces a texture. For Zircaloy cladding tubes, prism planes are preferentially aligned perpendicular to the axial (longitudinal) direction, which means that irradiation growth causes the axial length to increase and the cladding diameter and thickness to dimin-

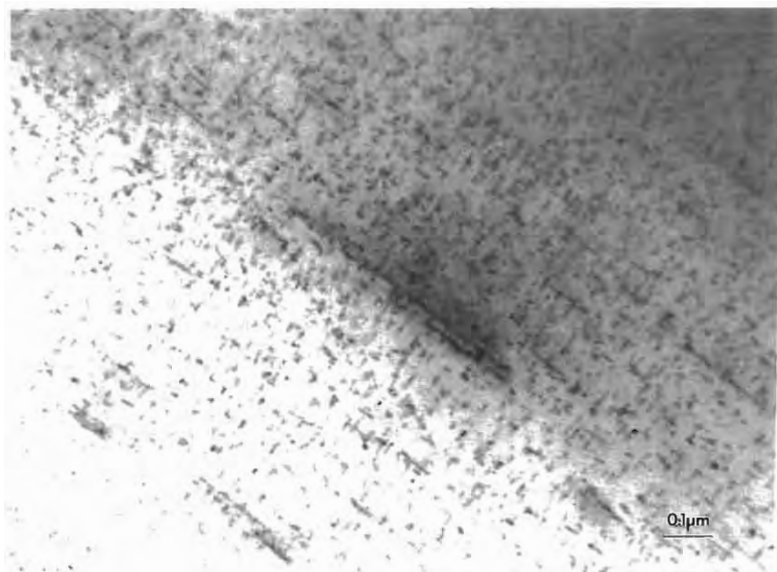


Figure 7-20. β -Nb precipitation in the α phase of Excel alloy (micrograph courtesy of R. W. Gilbert, AECL, Chalk River)

ish. Besides the possibility of failure by bowing in restricted rods (Franklin and Adamson, 1988), this has an impact on design and safety, the growth distortions setting operational burnup limits.

A considerable amount of experimental data has been gathered on this phenomenon (Rogerson, 1988), which will be briefly summarized here. Irradiation growth is influenced by microstructural variables such as amount of cold work, residual stresses and alloying additions, as well as by irradiation variables such as flux and temperature.

Figure 7-21 shows the influence of cold work and temperature on irradiation growth (Adamson, 1977). The growth strain in cold-worked material follows in general a constant linear slope with fluence, which is higher at higher temperatures. Annealed material has considerably lower strain rates, at least in the initial part of irradiation exposure. However, after a

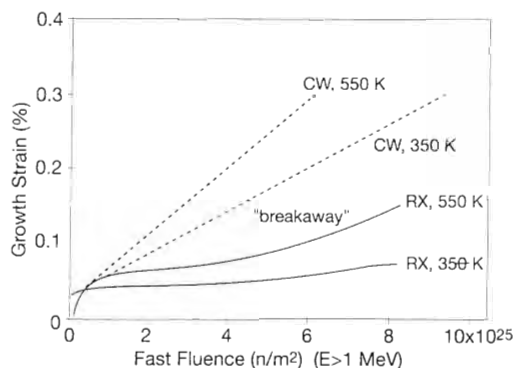


Figure 7-21. Growth strain versus fluence for different amounts of cold work, at several irradiation temperatures from Rogerson (1988). The dashed lines show the growth strain for cold-worked (CW) material: the strain is nearly linear with fluence and increases with temperature. The solid lines show the growth strain for annealed material: the growth rates are noticeably smaller than in cold-worked material, and also increase with temperature. After the "breakaway" fluence, growth rates in annealed material are comparable to those of cold-worked material. "Breakaway" growth in annealed materials has been linked to the development at that fluence of $\langle c \rangle$ -component dislocations (see Fig. 7-18).

fluence of about $3 \times 10^{25} \text{ n} \cdot \text{m}^{-2}$, there occurs the "breakaway phenomenon", the strain rates jumping to approximately the values observed in cold worked materials (Fidleris, 1988). The observation of breakaway growth has been linked to the development of $\langle c \rangle$ -component dislocations (Holt and Gilbert, 1983, 1986).

In general, when a high dislocation density exists, it dominates the growth behavior, which is then linear and steady state. According to rate theory (Wiedersich, 1972), this corresponds to a sink-dominated regime, where most of the defects created are lost to sinks, in this case dislocations. Transient behavior is observed in annealed materials or at the start of irradiation. When breakaway occurs, the observed growth rates are characteristic of a sink-dominated regime, as seen in Fig. 7-21.

Alloying elements can also have an effect on the growth rates. It has been suggested (Griffiths, 1988) that impurity elements, including Fe, stabilize embryo $\langle c \rangle$ -component loops, enabling the development of $\langle c \rangle$ -component dislocations referred to above. As noted in Sec. 7.2.3.2, iron enhances Zr self diffusion, which is another possible mechanism of enhancing growth, by enhancing point defect motion to dislocations. The influence of Sn has been measured by Zee et al. (1984): it was found that Zr-0.1% Sn grows considerably more than Zr-1.5% Sn. It is possible that this is a consequence of iron atom trapping by Sn atoms, thereby precluding Fe from enhancing growth. Recently, a new group of alloys with low Sn content, notably Zirlo (Boman et al., 1991) and the Russian alloy Zr 1% Nb 1% Sn 0.4% Fe (Nikulina et al., 1993) have shown noticeably reduced irradiation growth.

Irradiation growth is due to the partitioning of interstitials and vacancies to dif-

ferent sinks that are anisotropically distributed in the material. Those sinks can be cold-work or irradiation-induced dislocations of $\langle a \rangle$ or $\langle c \rangle$ or $\langle c + a \rangle$ character, and grain boundaries of different orientations. One example is the formation of either interstitial loops on $\langle a \rangle$ -planes or vacancy loops on $\langle c \rangle$ and $\langle c + a \rangle$ -planes, or both, as initially proposed by Buckley (1961). Buckley's original model gave

$$\dot{\epsilon}_x \propto 1 - 3F_x \quad (7-1)$$

where $\dot{\epsilon}_x$ is the strain rate due to growth in direction x and F_x is the resolved fraction of basal planes in the direction x . Since basal loops were initially not observed in irradiated material, alternative models were proposed that included other vacancy sinks such as grain boundaries (Carpenter and Northwood, 1975), or considered the effect of anisotropic defect migration (Woo, 1988).

Holt (1988) has presented a rate theory calculation that includes anisotropic point defect migration, texture effects, and all the point defect sinks proposed in previous models. It is found that growth in cold worked samples can be explained by a partitioning of vacancies to $\langle c + a \rangle$ -network dislocations and interstitials to $\langle a \rangle$ -type dislocations, while the accelerated growth observed in annealed material is due to the partitioning of vacancies to newly formed $\langle c \rangle$ -type loops and interstitials to $\langle a \rangle$ -type loops. In order to rationalize the linear growth rate at 350 K, a vacancy migration energy less than 0.7 eV is necessary, as initially shown by Buckley et al. (1980). This supports the Fe-enhanced vacancy migration mechanism mentioned in Sec. 7.2.3.2. Holt was also able to explain the simultaneous contraction along the longitudinal and transverse directions observed in some specimens as a grain size effect, operational when grain size falls below 1 μm in

highly oriented grains. The parameters adjusted to the behavior of Zircaloy were then used to successfully predict the growth of Zr-2.5% Nb (Holt and Fleck, 1991).

7.3.1.5 Irradiation Creep

Irradiation creep refers to the slow deformation under an external stress, experienced by a material under irradiation. In anisotropic materials, such as Zr, creep has always to be separated from growth in experimental situations. A convenient way to do this is to assume that creep and growth are linearly additive and define the irradiation creep strain as the additional strain that results when the deformation process takes place under an external stress. The creep strain is then the total strain minus the growth strain.

As shown in Fig. 7-22, the creep deformation rate of Zr alloys is increased under neutron flux. Due to the objective of using Zr alloys in reactor, this phenomenon has been subject to a large amount of experimental work, reviewed by Fidleris (1988),

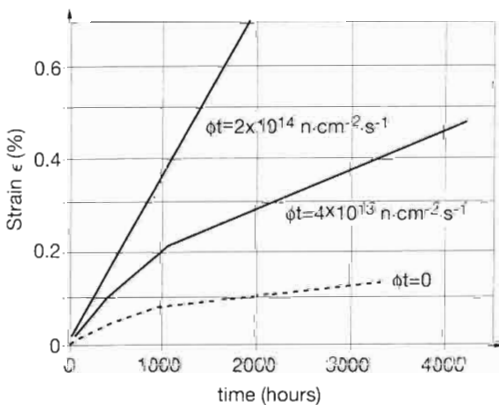


Figure 7-22. Diametral creep of RX Zircaloy under internal pressure (330 °C, $\sigma_H = 150$ MPa). The irradiation affects both the primary and the secondary creep, and the creep rate is increased in proportion to the dose rate.

in order to improve the knowledge of the parameters that control creep. Some of this work has been performed in materials test reactors, and some during detailed examinations of the behavior of structural material in power reactors. The experimental procedures used for those analyses, are based upon pressurized tube expansion, stress relaxation measurements of thin plates, tensile testing or shear testing (i.e., springs loaded in tension). The last method is a specific experiment designed to analyze the pure creep behavior. For example, Causey et al. (1984) were able to derive a contribution of about 30% $\langle c + a \rangle$ slip on the $1/3 \langle 11\bar{2}3 \rangle \{10\bar{1}1\}$ system in addition to the classical $\langle a \rangle$ -type basal slip by testing Zr-2.5 Nb in pure shear using compressed helical springs or twisted tubes at 573 K. They also showed a weak dependence of creep rate on dislocation density. Irradiation creep in Zircaloy-2 is anisotropic and dependent on texture as shown by Harbottle (1978).

For practical purposes and for the limited range of operating parameters, the irradiation creep strain rate may be described accurately with a simple equation of the form:

$$\dot{\epsilon} = A \cdot (\Phi t)^m \cdot \sigma^n \cdot e^{-Q/(RT)} \quad (7-2)$$

where the effect of flux, stress and temperature can be separated. The usual values of those exponents are $m = 0.6$ to 1, n close to 1. The fact that n is close to 1 means that large creep strains can be sustained without failure. The activation energy, Q , is low, in the range of 5 to 15 $\text{kJ} \cdot \text{mol}^{-1}$, i.e., 0.05 to 0.16 $\text{eV} \cdot \text{at}^{-1}$ (Franklin, 1982).

The task of finding a mechanistic model that explains irradiation creep in Zr alloys is a daunting one, in view of the complexity of the alloy, its inherent single-crystal and texture anisotropy, and the effect of the irradiation field. For example, since void

swelling is practically nonexistent in Zr alloys (Sec. 7.3.1.2), the standard rate theory model applicable to cubic metals coupling irradiation creep and void swelling (Brailsford and Bullough, 1972), cannot be used for Zr alloys. In addition, many of the parameters needed for mechanistic models, such as defect-defect interactions, are not known for Zr, further complicating the endeavor.

Matthews and Finnis (1988) recently reviewed the literature on mechanisms of irradiation creep. It is thought that deformation during irradiation creep occurs by a combination of dislocation climb and glide, the climb being controlled by the stress-modified absorption of point defects at dislocations. According to the so-called SIPA (stress induced preferential absorption) mechanism (Bullough and Willis, 1975), dislocations that have their Burgers vectors parallel to the applied uniaxial stress, preferentially annihilate interstitials than vacancies, leading to dimensional changes due to the dislocation climb itself and to the subsequent dislocation glide (Woo, 1979). Matthews and Finnis (1988), analyzing the possible origins for SIPA conclude that the elastodiffusion model proposed by Woo (1984) is the strongest candidate, since it is a first-order effect, involving the migration anisotropy of interstitials in an applied stress field.

The climb-assisted glide (I-creep) and SIPA mechanisms have recently been employed by Woo et al. (1990) to derive analytic expressions of their contribution to the single crystal stress compliance tensor and used a self-consistent model that treats each grain as an inclusion embedded in an anisotropic medium, for deriving expressions that relate the polycrystalline creep compliance tensor with that of a single crystal. Using a self consistent model, and a numerical technique, and using the ana-

lytic expressions derived by Woo et al. (1990), Christodoulou et al. (1992) derived the relative contributions of basal, pyramidal and prismatic slip systems to the total strain in Zircaloy-2 and Zr-2.5% Nb. It was concluded that $\langle a \rangle$ -type dislocations account for over 90% of the total strain.

The question of the influence of the microstructure is far from being resolved. Microstructural features that appear to influence creep are the grain shape (in the case of two-phase material the distribution of the β phase), and the dislocation structure. For example, when the grain size is relatively fine, the stress-induced anisotropic diffusion to grain boundaries can contribute significantly to the creep rate. Until the contribution of different mechanisms as a function of the microstructural features of the material is assessed, irradiation creep cannot be analyzed on the basis of a single creep mechanism.

7.3.1.6 Changes in Mechanical Behavior

Due to the high concentration of defects produced by neutron irradiation (point defects, dislocations), dislocation slip is inhibited and thus the yield strength increases after irradiation. This effect is rapidly saturated at a fluence which varies with irradiation temperature. For power reactors, the increase of the yield strength (YS) or UTS saturates above about 5×10^{24} to 10^{25} n m^{-2} . This saturation value is the same for both SR and RX Zircalloys. This is due to the fact that the initial microstructure no longer controls the deformation mechanisms. The increased density of dislocation loops controls the critical shear stress for dislocation glide. Since the increase in loop concentration under neutron irradiation saturates rapidly due to overlap of absorption volumes for interstitials and vacancies, the increase in yield strength saturates as well.

This increase in yield strength is associated with a reduction in ductility, affecting both the uniform elongation (through a reduction of the strain hardening exponent), and the total elongation, decreasing from about 20% to 2–4% (Morize, 1984). This effect is clearly illustrated in Fig. 7-23 from Price and Richinson (1978).

7.3.1.7 Charged-Particle Irradiation

For the sake of completeness, the use of charged-particles (electrons and ions) for experimental and theoretical studies of ir-

radiation effects in Zr alloys is discussed in this section. The motivation for studying irradiation effects with charged-particles is several fold: firstly, because their displacement rates are orders of magnitude higher than under neutron irradiation, equivalent doses in dpa are achieved correspondingly faster; secondly, the effect of experimental variables such as temperature, particle type and dose rate can be studied with relative ease, and, finally, the irradiated samples are usually not radioactive, making them much easier to handle.

In general, neither the results obtained in such experiments have a one-to-one correspondence with the results from neutron irradiation nor should such close correspondence be expected in principle, as the irradiations are quite different. Electron irradiation differs from neutron irradiation both in the absence of collision cascades, and in that the electron beam is focused, causing a much higher electron flux and displacement rate. For ion irradiation, the principal difference is that the rate of ion energy loss per unit target thickness is much higher than that for neutron irradiation, which causes only a relatively thin layer close to the surface to be irradiated, albeit at a much higher dose rate. Since irradiation effects are dependent on the balance between irradiation damage and thermal annealing, any shift in the displacement rate can affect the observed effects. Also, bulk effects of neutron irradiation, such as irradiation-induced creep and growth, and irradiation hardening are difficult to study with near-surface irradiation. If, however, the characteristics of each type of irradiation are taken into account, then charged-particle irradiation can provide valuable information on the mechanisms of irradiation damage and microstructural evolution, which can be applied to neutron irradiation.

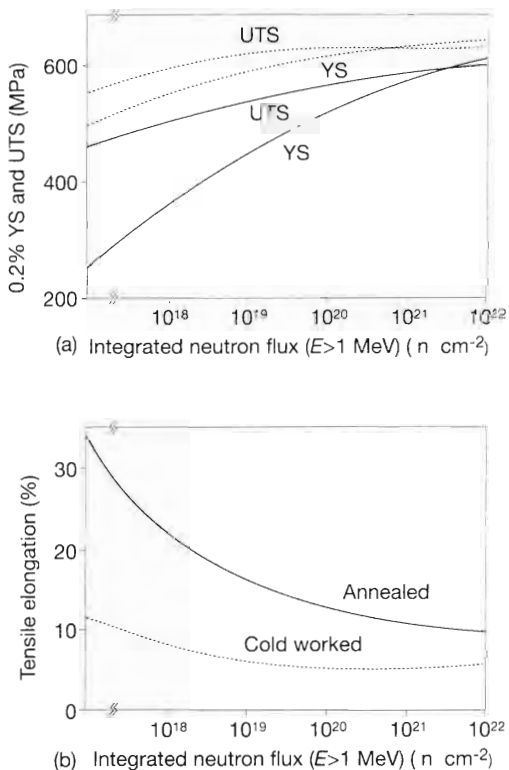


Figure 7-23. Effect of irradiation on the mechanical properties: (a) Due to defect build-up, the yield strength (YS) and fracture strength increase with dose, but the effect saturates at about $10^{24} n \cdot m^{-2}$ (dashed lines: 10% cold worked, solid lines: annealed yield strength). (b) The same effect occurs on ductility. In the case of cold worked material, the initial high dislocation density masks the effect of irradiation.

Most of the effects reviewed in Sec. 7.3.1 have also been studied with charged-particle irradiation, often with different results. Extensive studies of microchemical evolution in Zircaloy-2 and Zircaloy-4 under proton irradiation have been performed by Kai et al. (1990, 1992). It was found that proton irradiation may induce variations in the chemical composition of intermetallic precipitates and increase the solute content in the matrix. These changes appear to increase the nodular corrosion resistance of the alloy. Other investigations of the effect of irradiation on uniform oxidation in Zircaloy-2 and 4 have been conducted by Pêcheur et al. (1992) and are reported in Sec. 7.3.2.

Irradiation-induced segregation and precipitation has been observed in at least two different circumstances. Cann et al. (1992) have observed that 3.6 MeV proton irradiation of annealed Zr-2.5 Nb at 720 K–770 K to 0.94 dpa causes a fine dispersion of Nb-rich platelike precipitates to appear within the α grains that is absent upon equivalent heat treatment of a control sample, in agreement with the neutron irradiation results of Coleman et al. (1981), reported in Sec. 7.3.1.3. Segregation of tin and precipitation as β -Sn at the surface of thin Zircaloy-2 foils has also been reported after 5.5 MeV proton irradiation to 1 dpa at 350 K (Motta et al., 1992), a result that has not been observed after neutron irradiation of calandria tubes at equivalent temperatures.

Amorphization of intermetallic precipitates in Zircaloy-2 and 4 under charged particle irradiation has been extensively studied, both experimentally (Motta et al., 1989; Lefebvre and Lemaignan, 1989), and theoretically (Motta and Olander, 1990). The critical temperature for amorphization of Zr(Cr,Fe)₂ precipitates under electron irradiation was found to be 300 K

lower than under neutron irradiation. For Ar ion irradiation, although the critical temperature was similar to that under neutron irradiation, the transformation morphology was quite different, amorphization no longer starting at the precipitate matrix interface.

As mentioned above, bulk effects such as irradiation creep and growth and hardening, are more difficult to simulate with charged particle irradiation, but some attempts have been made, especially in the area of irradiation creep and growth. Parsons and Hoelke (1989) developed a “cantilever” beam method, which relates the irradiation-induced creep and growth of a cantilevered Zr beam to its deflection when exposed on one side to 100 keV Ne ion irradiation. The results of the experiment differed from those of neutron irradiation, but no detailed modeling effort has been undertaken as yet to rationalize the differences.

When both bulk and near-surface irradiation can be understood in terms of the atomic level mechanisms, then neutron irradiation can be simulated with charged particle irradiation. For example, formation of voids under electron irradiation was observed in a Zr sample that had been previously charged with He (Faulkner and Woo, 1980), and dislocation loop formation can be studied with electron irradiation (Woo et al., 1992). This last study incidentally, supported the idea that microstructural evolution in Zr alloys is affected by the large diffusion anisotropy, as mentioned in Sec. 7.2.3: irradiation-induced voids changed their shape under electron irradiation, preferentially shrinking in the $\langle a \rangle$ -direction, the expected direction of arrival of the interstitial flux.

7.3.2 Corrosion Behavior

7.3.2.1 General Corrosion Behavior

Zr alloys are highly resistant to corrosion in common media and are used for that reason in the chemical industry (Tricot, 1989). Those alloys are however not immune to oxidation and in the high temperature water environment found in a power reactor (280–340 °C at 10–15 MPa), corrosion and hydriding controls the design life of fuel rods and other components. Several international meetings have been organized to discuss this important design parameter, the latest ones having been reviewed by Franklin and Lang (1991).

In the early stages, a thin compact black oxide film develops that is protective and inhibits further oxidation. This dense layer of zirconia is rich in the tetragonal allotropic form, a phase normally stable at high pressure and temperature. As described in Fig. 7-24, the growth of the oxide layer thickness d , follows a power law, usually described by a quadratic relationship

$$d \propto \sqrt{t} \quad (7-3)$$

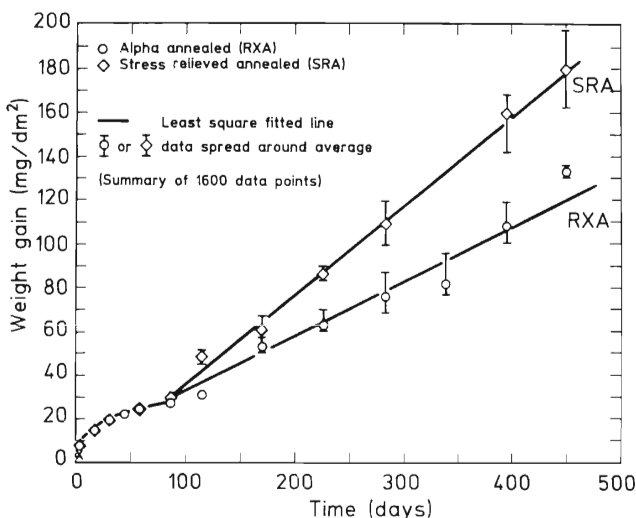


Figure 7-24. Uniform corrosion behavior of Zircaloy-4 in water at 633 K. The oxide thickness follows a power law up to a transition (1.5 to 2 mm thickness) and then remains linear. The metallurgical state of the material affects also the corrosion rate (Clayton and Fisher, 1985).

The activation energy of $130 \text{ kJ} \cdot \text{mol}^{-1}$ ($1.35 \text{ eV} \cdot \text{at}^{-1}$) for corrosion in the dense oxide regime (Billot et al., 1989) is equivalent to activation of the diffusion of oxygen in zirconia (Smith, 1969). Oxygen is considered to diffuse from the free surface of the oxide as O^{2-} , by a vacancy mechanism through the zirconia layer, and to react with the zirconium at the matrix–oxide interface, but recent studies support the fact that those ions diffuse mostly through grain boundaries (Godlewski et al., 1991).

For very thin oxide layers, the zirconia grows in epitaxy on the metallic zirconium (Ploc, 1983). The Pilling–Bedworth ratio, or ratio of the oxide volume to the parent metal volume, is equal to 1.56 for zirconia. Thus as the oxide grows, the stress buildu due to the volume expansion associated with oxidation induces a preferential oxide orientation that reduces the compressive stresses in the plane of the surface (David et al., 1971). This gives rise to various fibrous textures. Those compressive stresses are one of the factors that explain the stabilization of the tetragonal form of zirconia in this layer. A chemical effect of the alloying elements could also be invoked to explain that stabilization.

As the oxidation proceeds, the compressive stresses in the oxide layer cannot be counterbalanced by the tensile stresses in the metallic substrate and plastic yield in the metal limits the compression in the oxide. The tetragonal phase becomes unstable and the oxide transforms to a monoclinic form (Godlewski et al., 1991). This martensitic-type transformation is associated with the development of a very fine interconnected porosity that allows the oxidizing water to access closer to the corrosion interface (Cox, 1969). The size of those pores has been measured to be very small: Cox (1968) has used a modified mercury porosimeter to determine pore sizes smaller than 2 nm. His work has been confirmed by nitrogen absorption kinetics to pore sizes smaller than 1 nm, corresponding to a volume fraction of the order of 1% (Ramasubramanian, 1991). Once this transition has occurred, only a portion of the oxide layer remains protective. The corrosion kinetics are therefore controlled by diffusion of oxygen only through the dense protective oxide layer next to the metal substrate. Since the thickness of this layer remains constant, in the range of 1 μm (Garzarolli et al., 1991), the corrosion rate is constant after this transition (Fig. 7-24).

In this dense oxide layer the structure of the zirconia, which controls the posttransition corrosion kinetics, is complex and still under discussion. Starting from the metal-oxide interface, a very thin layer of amorphous oxide has been reported under particular conditions, about 10 nm in thickness (Warr et al., 1991). The existence of epitaxy shows that this layer, if present, should not be continuous. It is followed by a zone of very small zirconia crystallites, 10–20 nm, that become larger in diameter and columnar in shape further into the oxide layer (Bradley and Perkins, 1989).

For thick oxide layers, in excess of 50 μm , the oxide may spall, leaving zirconia particles free to flow in the cooling water, and giving rise to a much thinner oxide film. On the one hand, this process could be beneficial since it reduces the metal-oxide interface temperature, which is the parameter controlling oxidation kinetics. However, design considerations on remaining cladding thickness after oxidation does not allow for massive spalling in commercial reactors. Other undesirable consequences of spalling are the buildup of activity in the coolant and safety considerations, since those particles can interfere with the functioning of valves.

In BWRs, as shown in Fig. 7-25, nodular corrosion is the limiting design consideration. This behavior, specific to the boiling water reactor, can be reproduced by testing alloys in steam at 500°C (Schemel, 1987). Several mechanisms have been proposed for the nucleation of those nodules, leading to various possible sites for nodule nucleation: metallic matrix grain boundaries, local rupture of the continuous dense oxide at an early stage of growth, local variations in composition and precipitate densities or crystallographic orientation of clusters of grains (Charquet et al., 1989b; Ramasubramanian, 1989). As the corrosion progresses, the nodules grow in size and thickness and their number density increases leading to a complete coverage of the metal. The β quench structure described in Sec. 7.2.2.2 significantly improves the resistance of Zircaloy-4 to nodular corrosion, however as higher burnups are reached uniform corrosion could then become a problem.

7.3.2.2 Oxidation of the Precipitates

Since most of the metallic alloying elements present in Zircalloys are added for

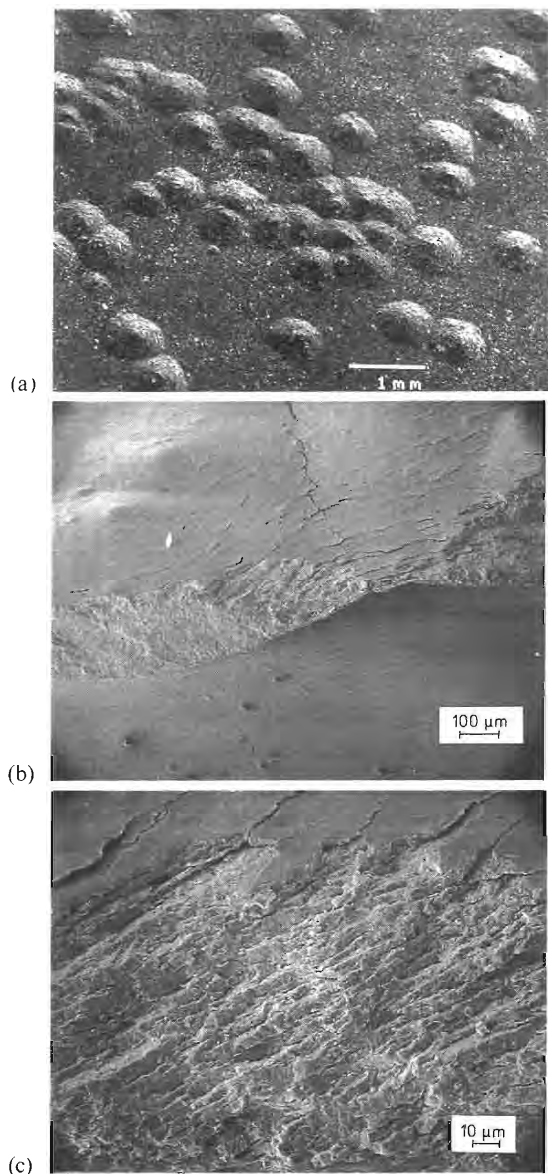


Figure 7-25. (a) Typical aspect of nodular corrosion of Zircaloy-4 obtained in a 500°C steam test. (b) Higher magnification of a cracked nodule in Zircaloy-4, obtained during a 10.3 MPa steam test at 500°C for 25 h, showing the extensive oxide cracking associated with the process. In addition to circumferential cracks in the flanks of the nodules, a vertical crack can also be seen running between the nodules [Courtesy of NFIR (Nuclear Fuel Industry Research Group)]. (c) Greater detail of the nodule, showing that the upper portion of the nodule consists of a series of parallel, cracked, oxide layers (Courtesy of NFIR).

improving corrosion resistance, the mechanism of their interaction with the oxidation front is of great importance. Due to the fine structure of the precipitates no specific observation of this process was available until recently, when a few studies have been performed using advanced STEM. It was shown that the precipitates are incorporated in metallic form into the oxide layer, and oxidize only afterwards, deeper into the oxide layer. In particular, iron has been shown to remain unoxidized in the dense oxide layer (Garzarolli et al., 1991; Pêcheur et al., 1992). The precipitates slowly release part of their iron in the oxidized matrix so oxide chemistry changes as the oxidation proceeds. It is found that the oxidation of iron coincide with the oxide transition from tetragonal to monoclinic.

Also, some of the crystalline intermetallic precipitates are found to be amorphous after incorporation into the oxide layer (Pêcheur et al., 1992). This transformation is not caused by irradiation since those are also observed in nonirradiated oxidized material. The crystal-to-amorphous transformation in the oxide layer could be caused by changes in chemistry, notably hydrogen intake (the nearest neighbor distance in the amorphous phase is bigger than in the corresponding precipitates amorphized by irradiation in the Zr matrix).

The effect of the release of iron in the oxide is still under consideration. A correlation has been found between the oxidation of the precipitates and the tetragonal-to-monoclinic transformation of the zirconia, but without clear knowledge of its origin (Godlewski et al., 1991). A chemical effect on the stabilization of the tetragonal phase of the oxide may be present.

An additional point is the role played by the precipitates as possible short circuits

for the electron current in the oxide film. In order to balance the charges transported by the O^{2-} ions across the film, electrons have to flow from the metal to the water. As zirconia is a good insulator, metallic precipitates could enhance this flow and be sites of preferential corrosion, a process considered for nodule nucleation (Cox, 1989).

A full description of the role played by the precipitates in the oxidation process is still not available. To date only partial, and often unexplained, observations have been made. For instance, a surprising observation is the opposite impact of precipitate size on corrosion rate in PWR's and BWR's as reported by Garzarolli and Stehle (1986). As seen in Fig. 7-26, the best microstructure for resisting localized corrosion in a BWR consists of fine precipitates (diameter below $0.15 \mu\text{m}$), whilst in PWR's, precipitates smaller than $0.1 \mu\text{m}$ increase the uniform corrosion rate.

7.3.2.3 Water Radiolysis

The interaction of irradiation particles (neutron, gamma, beta) with the coolant water leads to the formation of radiolytic oxidizing species, that are assumed to be responsible for the large increase in corrosion rate of Zr alloys in reactor, compared to similar out-of-reactor conditions.

Water radiolysis in the reactor core has been analyzed in great detail with the objective of knowing the steady state concentration of the radiolytic species during irradiation and their possible effect upon the zirconium corrosion rate (e.g., Burns and Moore, 1976). The main process of radiolysis is an instantaneous decomposition of the water molecules by interaction with the electrons in spurs (small volume of high interaction along the path of the electron), giving birth to metastable species that re-

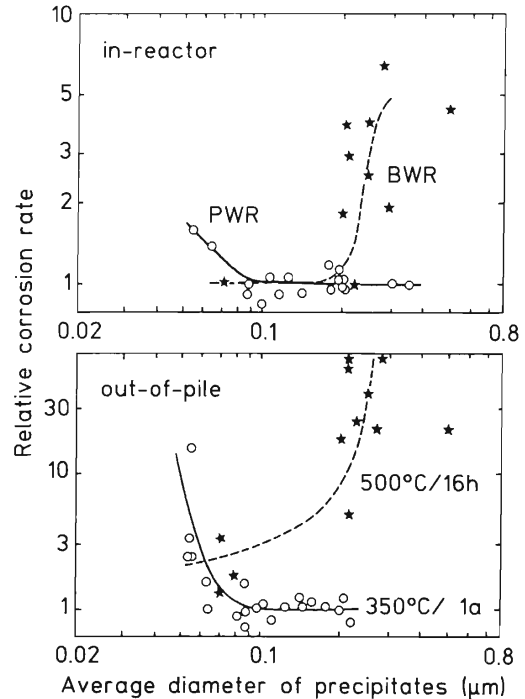


Figure 7-26. Influence of precipitate size on localized and uniform corrosion: The optimal microstructure for corrosion resistance is strongly dependent on corrosion conditions (Garzarolli and Stehle, 1986).

combine in a large variety of possible ways. The complexity of the recombination reactions can be illustrated by the large number (35 to 40) of reactions to be considered, each with its own rate. The concentrations of the intermediate and final products depend strongly on irradiation rate and initial conditions and therefore, local changes in irradiation intensity lead to drastic changes in the concentrations of radiolytic species. Some species appear for very short times as intermediate steps to long-lived species (Lukas, 1988). Computer programs are thus used for the computation of the evolution of those species versus initial chemical and irradiation conditions (Buxton and Elliott, 1991).

One way to decrease the build-up of oxidizing radiolysis products is to add hydro-

gen to the cooling water. Then a general reduction of stable radiolytic species occurs and a reduction in corrosion rate of thin oxide ensues. However this effect is not as efficient in boiling conditions compared to pressurized ones, due to the segregation of H_2 in the steam phase (Ishigure et al., 1987).

Radiolytic enhancement of corrosion can also occur in the case of PWR's, in post transition thick oxide films, or during corrosion testing of coupon specimens in a reactor corrosion loop. There, although no steam is expected to be present, the water chemistry in the pores of the thick oxide should be much like that present in BWRs, i.e., a two-phase regime (Johnson, 1989).

Some particular cases of localized corrosion enhancement have recently been linked to an increase in metastable oxidizing species due to β -radiolysis. The irradiation enhancement of corrosion is well observed for thick oxide films, where a three- to four-fold enhancement is commonly seen (Marlowe et al., 1985).

The reported occurrences are characterized by the presence of dissimilar materials in the vicinity of the corroding material. As recently reviewed, enhanced corrosion has been observed in front of stainless steel, copper cruds, platinum inserts and in the case of gadolinia bearing poison rods (Lemaignan, 1992). In all the reported cases, strong β emitters are present and the local energy deposition rates of those particles within the coolant are much larger than the bulk radiolysis contribution due to the neutrons and gammas. Thus, in reactor, the local intensity of the radiolysis has to be considered, as it will change the local chemistry for alloy corrosion.

In addition to the radiolysis described above, corresponding to chemical evolution by reaction in the bulk, specific considerations should be given to the fact that

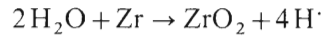
the pores have a large surface to volume ratio, leading to additional reactions at the surface of the pores, instead of a recombination between them as in the bulk. For instance, the H_2O_2 molecules can be adsorbed on the surface of the pores leading to the reaction:



instead of recombining in two steps with $2H$ as the standard back reaction to water after radiolysis. This leads to a higher oxygen potential at the surface of the ZrO_2 , giving a higher corrosion rate.

7.3.2.4 Hydrogen Pickup

During oxidation of Zr alloy components in reactors or in autoclaves, the reduction of water by the Zr alloy follows the general reaction scheme:



As described above, the reaction proceeds in several steps and the oxidation progresses at the metal-oxide interface by diffusion of O^{2-} ions through the oxide. The reduction of the water molecules at the coolant-oxide interface releases hydrogen as radicals $H\cdot$. They are chemically adsorbed at the tips of the oxide pores and their evolution controls the behavior of the hydrogen. Most of them recombine, creating hydrogen molecules that escape through the pore and dissolve into the coolant. A limited amount can ingress in the oxide and diffuse through to the metallic matrix and then react with Zr for the formation of hydrides, when the terminal solid solubility is exceeded. Corrosion experiments performed using tritium-doped water have shown that the H dissolved in the coolant is not trapped by the matrix, but that radicals obtained dur-

ing the reduction of water are necessary for hydrogen pick-up (Cox and Roy, 1965).

The diffusion coefficient of H in ZrO_2 has been measured with difficulty because of its very low value and because of the contribution of grain boundary diffusion and surface diffusion to diffusion in the pores of the oxide. Recent measurements by Khatamian and Manchester (1989) have confirmed earlier results in the range of 10^{-17} to $10^{-15} \text{ m}^2 \cdot \text{s}^{-1}$ at 400°C , depending on the condition of measurements and chemical composition of the alloy on which the oxide is grown. With such low values, the penetration of H in the oxide is limited, and the zirconia layer is indeed protective with respect to H ingress.

Care should be taken not to introduce catalyzers of the hydrogen molecule dissociation reaction that could enhance H pick-up (or hydrogen uptake) – i.e., the fraction of the hydrogen produced by reduction of water that is trapped into the Zr alloy. In that regard, Ni additions are to be avoided. This is the main reason for suppression of that element in Zircaloy-4. By reducing Ni, hydrogen pick-ups are generally in the range of 15% or less for standard PWR fuel cladding. BWR values tend to be around 20%.

In the case of CANDU pressure tubes, another mechanism of H pick-up has to be considered: the H in solution within the coolant diffuses through the stainless steel end fittings either directly into the pressure tube, or into the annulus gap. In the latter case it is then in contact with the outer part of the pressure tube. In order to avoid interaction with the pressure tube, a remaining ZrO_2 layer has to be maintained. The size of the protective oxide is controlled by O dissolution into the metal (Cheadle and Price, 1989), and therefore oxidizing agents are added to the gas annulus to replenish oxygen in the oxide layer and pre-

vent its degradation and enhanced H pickup (Urbanic et al., 1989).

One of the consequences of hydrogen ingress into Zr can be delayed hydride cracking (DHC) (Cheadle et al., 1987). The mechanism involves the ingress of hydrogen into a Zr-alloy component, its migration up a stress or thermal gradient and its concentration in the regions of low temperature or higher tensile stress. When the local concentration exceeds the terminal solid solubility (which happens first in colder regions), the hydride phase precipitates. As can be seen in Fig. 7-9, the terminal solid solubility of H in Zr is quite low, e.g., 80–100 ppm at 300°C . At low temperature, the hydrides crack when the stresses are high enough, the mechanism then being repeated until failure. The concentration of hydrogen in a tube stressed in bending can be seen in Fig. 7-27a, where the variation of hydride orientation along the tube thickness (and therefore stress state) is shown. The inner part of the tube is under tensile hoop stresses and the hydrides precipitate along radial planes, while in the outer part of the tube hydrides tend to precipitate along the habit plane, i.e., a more tangential direction. Figure 7-27b shows hydride formation at the tip of a crack due to local stress buildup. Pressure tubes in the CANDU Pickering 3 and 4 reactors failed by this mechanism.

With respect to this behavior, specifications may be required on cladding or pressure tube texture, usually measured by the morphology of hydride precipitation upon intentional addition of hydrogen.

7.3.3 Pellet–Cladding Interaction

Pellet–cladding interaction (PCI) associated with iodine intergranular stress corrosion cracking (IGSCC) is a mode of fuel rod failure that has been observed after

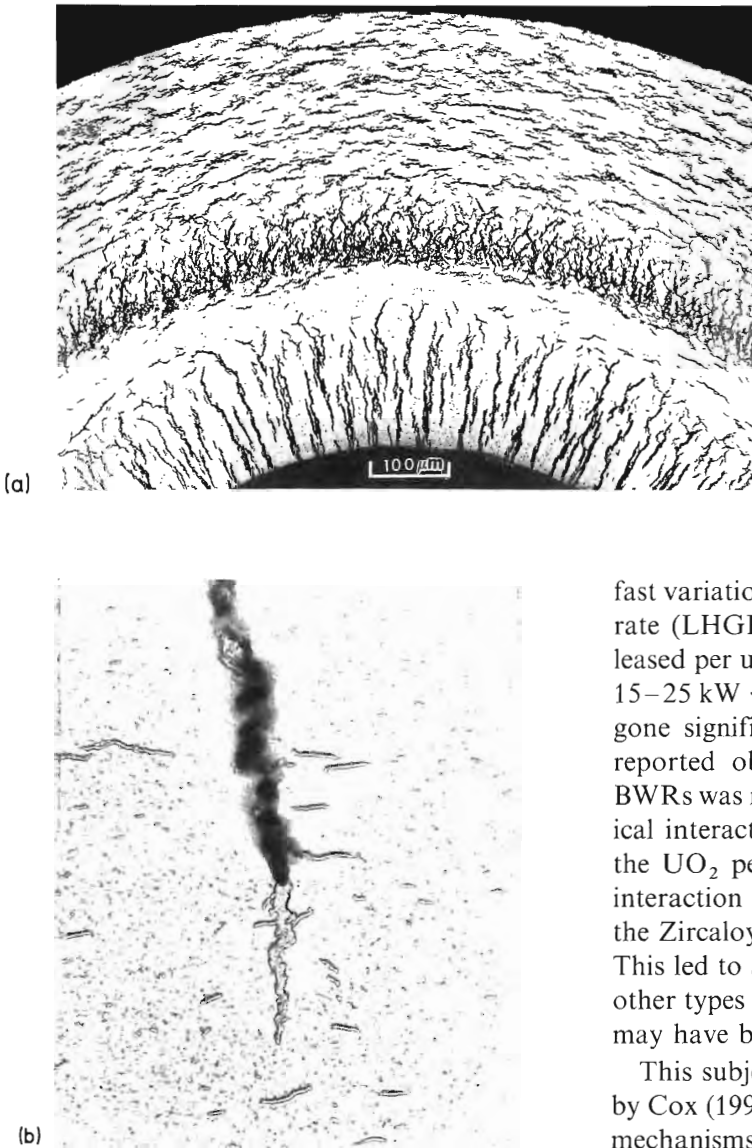


Figure 7-27. (a) Hydriding/D₂ pickup, showing stress dependence of hydride formation. The inner part of the tube is under tensile hoop stresses and the hydrides precipitate along radial planes, while in the outer part of the tube hydrides tend to precipitate along their habit plane, i.e., in a more tangential direction (micrograph courtesy of C. E. Coleman, AECL/Chalk River). (b) Hydride formation at a crack tip in Zr-2.5 Nb due to the local buildup of stresses (photo courtesy of D. Rogers, AECL/Chalk River).

fast variations in the linear heat generation rate (LHGR) (i.e., the thermal power released per unit length of fuel rod, typically $15\text{--}25\text{ kW}\cdot\text{m}^{-1}$), in fuel that has undergone significant burn-up (BU). The first reported observation of PCI failure on BWRs was rapidly diagnosed as a mechanical interaction between the cladding and the UO₂ pellet, associated with chemical interaction of some fission products with the Zircaloy cladding (Rosenbaum, 1966). This led to a spreading interest to identify other types of reactors where this problem may have been of concern.

This subject has been reviewed recently by Cox (1990), see also Chap. 3. The main mechanisms invoked to explain the failure are described schematically in Fig. 7-28. A combined contribution of stresses induced by fuel pellet expansion due to LHGR increase and the presence of an active corrosion agent, the iodine, created in the fuel rod as fission product, induces failure by stress corrosion cracking (SCC).

The occurrence of the problem led the international fuel community to set up large R & D programs. There were two main objectives:

(1) For practical purposes, design parameters were analyzed on integral tests on fuel rods:

Fuel rods of various design and irradiation histories were tested in irradiation devices of test reactors. After a short irradiation at the LHGR close to the one used in the power reactor, the irradiation power was increased at a given rate and the behavior of the rod was analyzed with respect to its capacity to support the change in LHGR without failure. This type of experiment gives information on the maximum power allowable for a fuel rod, usually expressed as a function of the BU. For fresh fuel rods, an open gap exists in operation and large power changes are acceptable: Maximum power levels

above $50 \text{ kW} \cdot \text{m}^{-1}$ are common. This limit decreases slowly with BU up to $20 \text{ GW} \cdot \text{d} \cdot \text{t}^{-1}$, when it stabilizes in the range of $40\text{--}45 \text{ kW} \cdot \text{m}^{-1}$. Various examples of the testing procedures used and of the results obtained can be found in the proceedings of a series of IAEA specialist meetings, e.g., IAEA (1982).

(2) For understanding mechanisms and for remedial aspects, analytical work was carried out in laboratories on the basic mechanisms involved:

The analytical work was focused on the SCC behavior of fuel cladding materials. This aspect of the problem is discussed in more detail here.

The stresses are induced by the thermal expansion of the pellet during power transients. During steady state operation, the pressure of the coolant causes the cladding to creep down to the fuel pellet. In addition, fuel swelling at low temperature, due to fission products, contributes to gap closure. In PWRs this phase may take a year or two, while BWRs keep their gap open longer.

Once the gap is closed, any change in pellet dimension is transferred to the cladding. For a standard power change, typically from 20 to $40 \text{ kW} \cdot \text{m}^{-1}$, the change in centerline temperature induces a thermal expansion of about 0.25% for each $10 \text{ kW} \cdot \text{m}^{-1}$. This strain is high enough to induce stresses close to or above the yield strength (Porrot et al., 1991). During the time at which the fuel is maintained at high power, a stress level of one half to two thirds of the yield strength and the presence of a corrosive agent are sufficient to initiate and propagate a crack that leads to fuel rod failure.

In addition to iodine (I), fission products such as cesium (Cs) and cadmium (Cd) were suspected early on as candidate corroding agents. Those elements are

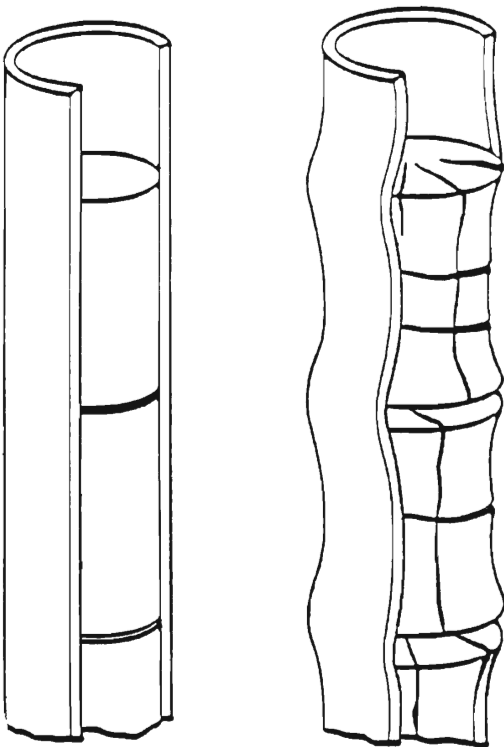


Figure 7-28. Cladding strain induced by pellet thermal expansion upon increase of linear heat generation rate (after Levy, 1974).

known to induce intergranular fracture of Zr alloy by a liquid metal embrittlement mechanism. The type of fracture surface morphologies was a main reason for rejection of those species. On the other hand, the higher fission yield of Cs compared to I, introduced a discussion on the availability of this agent for interaction with the stressed cladding, due to the low vapor pressure of iodine in equilibrium with solid CsI at fuel temperature. The intense radiolysis due to the fission recoils in the interior of the fuel rod, has been shown to be able to increase the effective pressure of iodine in equilibrium with CsI to a level where SCC has been shown to occur (Konashi, 1984).

In order to understand the mechanisms involved in iodine-induced SCC of zirconium alloys, tests were performed on various types of materials in different conditions. The most frequent tests were either constant load tests, where the time to failure is expressed versus the applied stress in the iodine environment, or constant strain rate tests, where the reduction in ductility due to iodine is analyzed (Brunisholtz and Lemaignan, 1987). A reduction in time or strain to failure is observed and several parameters have been shown to be of importance: internal surface condition, metallurgical state and texture of the material.

In an early experiment performed by Peehs et al. (1979), the effect of basal plane orientation with respect to stress, was rec-

ognized to be critical: machining a tube out of a thick Zircaloy plate, they were able to obtain an angular variation of the texture around this test sample. After testing under iodine, the density of cracks was found to be strongly dependent upon the relative orientation of the basal planes. The densities of cracks were higher when the c -planes were in the direction of the crack growth (Fig. 7-29).

To explain those results, the characteristic aspect of SCC fracture surface has to be analyzed in order to explain the mechanism of rupture. Figure 7-30 shows a SEM view of a recrystallized Zircaloy tested in tension in iodine environment. The fracture surface is transgranular and consists mostly of large transgranular pseudo cleavage areas where fracture occurs by SCC interconnected by fluted walls in which plastic deformation is evident. Crystallographic analysis of the pseudo-cleavage areas have shown that they consist of basal planes, while the fluted walls are located on prismatic planes. The propagation of the SCC fracture surface on the basal plane is enhanced by the strong decrease in surface free energy of this plane when iodine is adsorbed on it (Hwang and Han, 1989). Fluted walls are obtained by plastic deformation on the primary slip system to connect the different pseudo-cleavage planes in a ductile type rupture mode.

Due to the perpendicular directions of the slip on the prismatic plane and of the

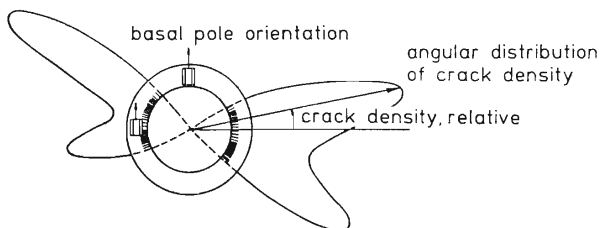


Figure 7-29. Density of crack developed during an iodine SCC test of a tube machined out of a plate. Along the circumference, the orientation of the $\langle c \rangle$ -planes changes from radial to tangential. The cracks tend to develop when they can grow following the c -planes (Peehs et al., 1979).

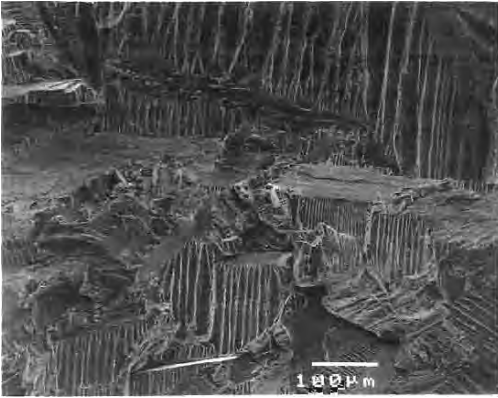


Figure 7-30. Fracture surface of RX Zr by SCC cracking in iodine. The crack grows by pseudo-cleavage on the basal plane and those brittle areas are connected by fluted prismatic planes on which ductile rupture occurred.

pseudo-cleavage on the basal plane, no plastic deformation can contribute to the reduction of tensile stresses on this plane. Thus the relative orientation of the basal plane with respect to the applied tensile stresses is a critical parameter, and the effect of the texture is remarkable. Constant stress and fracture mechanics tests have indeed shown that when the c -type planes tend to be aligned with the macroscopic crack surface, the susceptibility to SCC increases (Knorr and Pelloux, 1982). For cladding tubes, where the tensile stresses are the hoop stresses due to the pellet expansion, the best texture corresponds to a maximum intensity of the c -direction in the radial direction. Figure 7-31 shows the susceptibilities to SCC in iodine environment of a series of claddings with different textures but processed from the same ingot, plotted as a function of the angle between the maximum intensity of the c -poles and the radial direction (Schuster and Lemaignan, 1992). It is clear that the more the basal planes are aligned with the radial direction, the less susceptible is the cladding to SCC. The stress intensity fac-

tor (K_{ISCC}) for SCC crack growth was found to be dependent upon the same parameters. Measurements on different orientation of cracks in Zircaloy plates or crack propagation through the wall of different claddings gave K_{ISCC} in the range of 3.5 to 6 $\text{MPa} \cdot \text{m}^{1/2}$. The lowest K_{ISCC} corresponds to the highest orientation of the c -planes in the propagation direction.

Due to the fast SCC crack growth rates measured, in the range of 1 to 10 $\mu\text{m} \cdot \text{s}^{-1}$, the nucleation step is the longest part of the SCC lifetime (Brunisholtz and Lemaignan, 1987); therefore it controls the overall SCC behavior. The intermetallic precipitates have been suggested to be places of crack initiation as preferential sites for iodine corrosion (Kubo et al., 1985). Another action of the precipitates related to crack initiation would be, in the case of intergranular precipitates, the inhibition of grain boundary sliding thereby causing a local stress buildup which enhances crack formation. The last mechanism to be considered is the large strain incompatibilities, from one grain to the next one during plastic deformation, found in Zr alloys, due to the limited number of slip systems available. Due to the fact that plastic deformation on the prismatic system does not relax

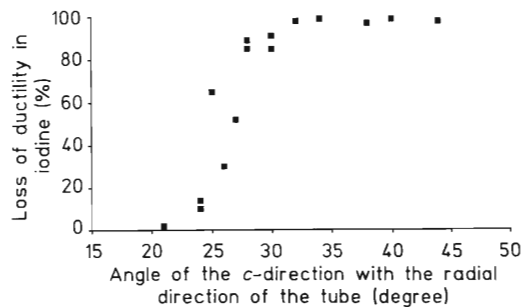


Figure 7-31. Effect of texture on SCC susceptibility in iodine. The same alloy was used to process tubes of different textures, and the susceptibility to I-SCC is found to decrease for a more radial texture.

stresses for crack formation on the basal plane, those incompatibilities are efficient mechanisms for crack initiation (Kubo et al., 1985).

An early solution to the PCI problem was to reduce the power change rates in order to reduce the hoop stresses in the cladding by relaxation during the loading time. Specific procedures have been implemented with success, but the drawback is a loss of power availability, driving R & D work to a solution obtained by fuel design. For practical purposes, remedies have been found and tested to avoid PCI type failures. In the reactors most prone to this phenomenon, advanced claddings have been developed with success. For the CANDU reactors, where the fuel bundle maneuvers during on power refuelling induce large local changes in LHGRs, the "CANLUB" design consists of an internal coating of graphite in internal surface of the cladding (Wood and Kelm, 1980). "Barrier" fuel rods for BWRs contain an internal layer of pure recrystallized Zr that is coextruded with the Trex and cold rolled with the base Zircaloy metal to obtain a perfect metallurgical bond (Rosenbaum et al., 1987).

7.4 Challenges

At the end of this review of the current knowledge of the behavior of Zr alloys for nuclear application, it may be of interest to list some open questions for a better understanding of the physical mechanism involved in specific properties. Indeed although the use of Zr alloys has proven a good engineering solution, several properties are still subject to a poor scientific understanding of their origins. Among them, the following topics, related to deformation, point defects and corrosion, can be

proposed for further basic work:

- Due to the high anisotropy of the Zr matrix, and the limited number of deformation systems available, thermo-mechanical processing gives rise to the textures described in Sec. 7.2.3.3. Although the texture obtained after a given thermo-mechanical processing route is well known, its accurate prediction is impossible today for a new alloy or a major change in processing. Improvement in the understanding of the deformation of Zr alloys could be focused on the different shear and twin systems active as a function of temperature, stress distribution, alloy composition and structure, irradiation fluence. The knowledge of the critical shear stresses for their activation is extremely limited. If well measured, a consequence would be a better evaluation of the local strain during plastic deformation or thermal treatments (e.g., strain incompatibility, local crystal rotation, texture development). In addition the interaction of the cold-work dislocations with the irradiation defects is probably responsible for the reduction of strain anisotropy after irradiation, by activation of new slip systems. This has to be analyzed.

In connection with in-reactor deformation, the growth phenomenon is one of the limiting design considerations of the structural components. The reason for the occurrence of the $\langle c \rangle$ -type dislocations after a fluence of $3 \times 10^{25} \text{ n} \cdot \text{m}^{-2}$ and their impact on growth, is still an open question, the contribution of minor alloying elements in stabilizing those dislocations being suspected. Detailed understanding of this process is highly desirable.

- In the field of point defects, one should consider the alloying elements in solid

solution and irradiation-induced point defects. The complex diffusion behavior of the foreign atoms, either in substitution or as interstitials, leads one to suspect many cases of solute–defect interaction, giving rise to irradiation induced segregation or accelerated diffusion. With respect to that behavior, the current effort to compute the formation and migration energies of different defect configurations involving one or several atoms, using molecular dynamics and to obtain experimental data on point defect energies and mobilities should be continued. In particular, the anisotropy of diffusion is an important parameter for irradiation growth and creep behavior.

- For corrosion, although a general scheme of the phase transformation in the zirconia responsible for the transition is available, the details of the mechanisms are still to be described accurately. In particular, the effect of alloying elements and their distribution in the Zr matrix is of importance. The localized corrosion rate enhancement under irradiation can be correlated to local radiolysis due to β flux, but a quantitative model is still unavailable. In the same area, in order to reduce the hydrogen pick-up during corrosion, the process should be studied in more detail, in particular the transport mechanism through the zirconia film.

Zirconium alloys are paralleled only by steels in the large amount of irradiation data available. However, their irradiation behavior is more complex than that of stainless steel, due to the anisotropy of the .c.p. Zr and to the behavior of the alloying elements. The increasing amount of basic data available leads to the hope that the prediction of the in-reactor behavior will

soon come from mechanistic models based on a more fundamental understanding of the processes involved, rather than from empirical correlations.

7.5 Acknowledgements

This work was completed while one of us (ATM) was at AECL/Chalk River Laboratory, and this review was enriched by the comments and criticism from several scientists there: Vince Urbanic and Malcolm Griffiths carefully reviewed the manuscript; and Rick Holt, Gavin Hood, Nick Christodoulou and Robert Ploc made special contributions to various specific sections.

Daniel Charquet, of Cezus, and John Harbottle of the Stoller Corporation also provided comments on the manuscript.

The authors sincerely thank all of them.

7.6 References

- Abriata, J. P., Bolcich, J. C. (1982), *Bull. Alloy Phase Diagrams* 3(1), 1710–1712.
- Abriata, J. P., Garces, J., Versaci, R. (1986), *Bull. Alloy Phase Diagrams* 7(2), 116–124.
- Adamson, R. B. (1977), *ASTM-STP 633*. Philadelphia, PA: Am. Soc. Test. Mat., pp. 326–343.
- Arias, D., Abriata, J. P. (1986), *Bull. Alloy Phase Diagrams* 7(3), 237–243.
- Arias, D., Abriata, J. P. (1988), *Bull. Alloy Phase Diagrams* 9(5), 597–604.
- Armand, M., Givord, J. P., Tortil, P., Tronlet, G. (1965), *Mém. Scient. Rev. Métall.* 62, 275–283.
- Asada, T., Komoto, H., Chiba, N., Kasai, Y. (1991), *9th Int. Conf. Zr Nucl. Ind., Nov. 1990, Kobe, Japan: ASTM-STP 1132*. Philadelphia, PA: Am. Soc. Test. Mat., pp. 99–118.
- ASTM (1990), *Standard B 353.89*. Philadelphia, PA: Am. Soc. Test Mat.
- Bacon, R. (1988), *J. Nucl. Mater.* 159, 176–189.
- Baig, M. R., Messoloras, S., Stewart, R. J. (1989), *Rad. Effects* 108, 355–358.
- Bangaru, N. V. (1985), *J. Nucl. Mater.* 131, 280–290.
- Bhanumurthy, K., Kale, G. B., Khera, S. K. (1991), *J. Nucl. Mater.* 185, 208–213.

- Billot, P., Beslu, P., Giordano, A., Thomazet, J. (1989), *8th Int. Conf. Zr Nucl. Ind., June 19–23, 1988, San Diego, CA: ASTM-STP 1023*. Philadelphia, PA: Am. Soc. Test. Mat., pp. 165–184.
- Boman, L. H., Kilp, G. R., Balfour, M. G., Schoenberger, G. (1991), *9th Int. Conf. Zr Nucl. Ind., Nov. 1990, Kobe, Japan: ASTM-STP 1132*, Philadelphia, PA: Am. Soc. Test. Mat., poster session.
- Bradbrook, J. S., Lorimer, G. W., Ridley, N. (1972), *J. Nucl. Mater.* 42, 142–160.
- Bradley, E. R., Perkins, R. A. (1989), *Proc. Tech. Com. Meet. IAEA: Fundamental Aspects of Corrosion in Zr-Base Alloys in Water Reactor Environments, Sept. 11–15, 1989, Portland, OR*, pp. 101–106.
- Brailsford, A. D., Bullough, R. (1972), *J. Nucl. Mater.* 44, 121–135.
- Brunisholz, L., Lemaignan, C. (1987), *7th Int. Conf. Zr Nucl. Ind.: ASTM-STP 939*. Philadelphia, PA: Am. Soc. Test. Mat., pp. 700–716.
- Buckley, S. N. (1961), *Properties of Reactor Materials and the Effects of Irradiation Damage: Litter, D. J. (Ed.)*. London: Butterworths, p. 443.
- Buckley, S. N., Bullough, R., Hayns, M. R. (1980), *J. Nucl. Mater.* 89, 283–295.
- Bullough, R., Willis, J. R. (1975), *Phil. Mag.* 31, 855–861.
- Burgers, W. G. (1934), *Physica* 1, 534–546.
- Burns, W. G., Moore, P. B. (1976), *Rad. Effects* 30, 233–242.
- Buxton, G. V., Elliott, A. J. (1991), *Proc. JAIF Int. Conf. Water Chem. Nucl. Power Plants, Apr. 22–25, 1991, Fukui City, Japan*.
- Carpenter, G. J. C., Northwood, D. O. (1975), *J. Nucl. Mater.* 56, 260–266.
- Cann, C. D., So, C. B., Styles, R. C., Coleman, C. E. (1992), *Precipitation in Zr-2.5 Nb Enhanced by Proton Irradiation*, presented at: *Conf. Microstructural Evolution Metals During Irradiation, Muskoka, Canada, Sept.–Oct. 1992*. To be published in *J. Nucl. Mater.* (1993).
- Causey, A. R., Holt, R. A., McEwen, S. R. (1984), *6th Int. Conf. Zr Nucl. Ind., June 28–July 1, 1982, Vancouver, Canada: ASTM-STP 824*. Philadelphia, PA: Am. Soc. Test. Mat., pp. 269–288.
- Charquet, D., Alheritière, E. (1985), *Proc. Workshop: Second Phase Particles in Zircalloys, Erlangen, F.R.G. Kerntechnische Gesellschaft*, pp. 5–11.
- Charquet, D., Hahn, R., Ortlieb, E., Gros, J. P., Wadier, J. F. (1989 a), *8th Int. Conf. Zr Nucl. Ind., June 19–23, 1988, San Diego, CA: ASTM-STP 1023*. Philadelphia, PA: Am. Soc. Test. Mat., pp. 405–422.
- Charquet, D., Tricot, R., Wadier, J. F. (1989 b), *8th Int. Conf. Zr Nucl. Ind., June 19–23, 1988, San Diego, CA: ASTM-STP 1023*. Philadelphia, PA: Am. Soc. Test. Mat., pp. 374–391.
- Cheadle, B. A. (1975), *The Physical Metallurgy of Zr Alloys, CRNL Report, 1208*.
- Cheadle, B. A., Alridge, S. A. (1973), *J. Nucl. Mater.* 47, 255–258.
- Cheadle, B. A., Price, E. G. (1989), *IAEA Tech. Com. Meet. Exch. Operational Safety Exp. Heavy Water Reactors, Feb. 20–24, 1989, Vienna, Austria, AECL 9939*.
- Cheadle, B. A., Coleman, C. E., Ambler, J. F. (1987), *7th Int. Conf. Zr Nucl. Ind., ASTM-STP 939*. Philadelphia, PA: Am. Soc. Test. Mat., pp. 224–240.
- Christodoulou, N., Causey, A. R., Woo, C. H., Klassen, R. J. (1992), *10th Conf. Zr Nucl. Ind., Philadelphia, PA, 1993: ASTM-STP 1175*. Philadelphia, PA: Am. Soc. Test. Mat., submitted.
- Clayton, J. C., Fischer, R. L. (1985), *Proc. ANS Topical Meet. Light Water Reactor Fuel Performance, Orlando, FL, April 21–24 1985*. La Grange Park, IL: ANS, pp. 3-1–3-5.
- Coleman, C. E., Gilbert, R. W., Carpenter, G. J. C., Weatherly, G. C. (1981), in: *Phase Stability Under Irradiation, AIME Symp. Proc.* Holland, J. R. et al. (Eds.). Metals Park, OH: Am. Inst. Mech. Eng.
- Cox, B. (1968), *J. Nucl. Mater.* 27, 1–47.
- Cox, B. (1969), *J. Nucl. Mater.* 29, 50–66.
- Cox, B. (1989), *Proc. Tech. Com. Meet. IAEA: Fundamental Aspects of Corrosion in Zr Base Alloys in Water Reactor Environments, Sept. 11–15, 1989, Portland, OR*, pp. 167–173.
- Cox, B. (1990), *J. Nucl. Mater.* 172, 249–292.
- Cox, B., Roy, C. (1965), *The Use of Tritium as Tracer in Studies of Hydrogen Uptake by Zr Alloys, AECL-2159*.
- David, G., Geschier, R., Roy, C. (1971), *J. Nucl. Mater.* 38, 329–339.
- Dawson, C. W., Sass, S. L. (1970), *Met. Trans. 1*, 2225–2233.
- Douglass, D. L. (1971), *The Metallurgy of Zirconium, Atomic Energy Review*, Vienna.
- Farrell, K. (1980), *Rad. Eff.* 53, 175–194.
- Faulkner, D., Woo, C. H. (1980), *J. Nucl. Mater.* 90, 307–316.
- Fidleris, V. (1988), *J. Nucl. Mater.* 159, 22–42.
- Franklin, D. G. (1982), *5th Int. Conf. Zr Nucl. Ind., Aug. 4–7, 1980, Boston, MA: ASTM-STP 754*. Philadelphia, PA: Am. Soc. Test. Mat., pp. 235–267.
- Franklin, D. G., Adamson, R. B. (1988), *J. Nucl. Mater.* 159, 12–22.
- Franklin, D. G., Lang, P. (1991), *9th Int. Conf. Zr Nucl. Ind., Nov. 1990, Kobe, Japan: ASTM-STP 1132*. Philadelphia, PA: Am. Soc. Test. Mat., pp. 3–32.
- Fuse, M. (1985), *J. Nucl. Mater.* 136, 250–277.
- Garzarolli, F., Stehle, H. (1986), *IAEA Symp. Improvements Water Reactors Fuel Tech. Utilization Stockholm, Sweden: IAEA SM 288/24*, pp. 387–407.

- Garzarolli, F., Seidel, H., Tricot, R., Gros, J. P. (1991), *9th Int. Conf. Zr Nucl. Ind., Nov. 1990, Kobe, Japan: ASTM-STP 1132*. Philadelphia, PA: Am. Soc. Test. Mat., pp. 395–415.
- Gilbert, R. W., Griffiths, M., Carpenter, G. J. C. (1985), *J. Nucl. Mater.* 135, 265–268.
- Godlewski, J., Gros, J. P., Lambertin, M., Wadier, J. F., Weidinger, H. (1991), *9th Int. Conf. Zr Nucl. Ind., Nov. 1990, Kobe, Japan: ASTM-STP 1132*. Philadelphia, PA: Am. Soc. Test. Mat., pp. 416–436.
- Griffiths, M. (1988), *J. Nucl. Mater.* 159, 190–218.
- Griffiths, M. (1989), *J. Nucl. Mater.* 165, 315–317.
- Griffiths, M., Gilbert, R. W., Carpenter, G. J. C. (1987), *J. Nucl. Mater.* 150, 53–66.
- Griffiths, M., Gilbert, R. W., Coleman, C. E. (1988), *J. Nucl. Mater.* 159, 405–416.
- Griffiths, M., Gilbert, R. W., Fidleris, V. (1989), *ASTM-STP 1023*. Philadelphia, PA: Am. Soc. Test. Mat., pp. 658–677.
- Gros, J. P., Wadier, J. F. (1989), *Proc. Tech. Com. Meet. IAEA: Fundamental Aspects of Corrosion in Zr Base Alloys in Water Reactors Environments, Sept. 11–15, Portland, OR*, pp. 211–225.
- Guibert, E. R., Duran, S. A., Bement, A. L. (1969), *ASTM-STP 456*. Philadelphia, PA: Am. Soc. Test. Mat., pp. 210–226.
- Harbottle, J. (1978), *Phil. Mag.* 38, 49.
- Holt, R. A. (1988), *J. Nucl. Mater.* 159, 310–338.
- Holt, R. A., Causey, A. R. (1987), *J. Nucl. Mater.* 150, 306–318.
- Holt, R. A., Fleck, R. G. (1991), *9th Int. Conf. Zr Nucl. Ind., Nov. 1990, Kobe, Japan: ASTM-STP 1132*. Philadelphia, PA: Am. Soc. Test. Mat., pp. 218–229.
- Holt, R. A., Gilbert, R. W. (1983), *J. Nucl. Mater.* 116, 127–130.
- Holt, R. A., Gilbert, R. W. (1986), *J. Nucl. Mater.* 137, 185–189.
- Hood, G. M. (1988), *J. Nucl. Mater.* 159, 149–175.
- Hood, G. M., Schultz, R. J. (1974), *Acta Met.* 22, 459–464.
- Hood, G. M., Zou, H., Schultz, R. J., Roy, J. A., Jackman, J. A. (1992), *J. Nucl. Mater.* 189, 226–230.
- Hwang, S. K., Han, H. T. (1989), *J. Nucl. Mater.* 161, 175–181.
- IAEA (1982), *Specialist Meeting on Power Ramping and Cycling Behavior of Water Reactor Fuel, Sept. 8–9, Petten, Holland: IWGFPT/14*.
- Ishigure, K., Takagi, J., Shiraishi, H. (1987), *Radiat. Phys. Chem.* 29, 195–199.
- Isobe, T., Matsuo, Y. (1991), *9th Int. Conf. Zr Nucl. Ind., Nov. 1990, Kobe, Japan: ASTM-STP 1132*. Philadelphia, PA: Am. Soc. Test. Mat., pp. 346–367.
- Johnson, A. B. (1989), *IAEA Tech. Com. Meet.: Fundamental Aspects of Corrosion of Zb-base Alloys in Water Reactor Environments, Sept. 11–15, Portland, OR: IWGFPT/34*, pp. 107–119.
- Jostsons, A., Kelly, P. M., Blake, R. G., Farrell, K. (1979), *Proc. 9th Symp. Effect Radiation on Materials: ASTM-STP 633*. Philadelphia, PA: Am. Soc. Test. Mat., pp. 46–61.
- Kai, J. J., Huang, W. I., Chou, H. Y. (1990), *J. Nucl. Mater.* 170, 193–209.
- Kai, J. J., Tsai, C. H., Hsieh, W. F. (1992), *15th ASTM Int. Symp. Effects Irradiation Mater. ASTM-STP 1125*. Philadelphia, PA: Am. Soc. Test. Mat., pp. 355–372.
- Khatamian, D., Manchester, F. D. (1989), *J. Nucl. Mater.* 166, 300–306.
- Kearns, J. J., Woods, C. R. (1966), *J. Nucl. Mater.* 20, 241–261.
- King, A. D., Hood, G. M., Holt, R. A. (1991), *J. Nucl. Mater.* 185, 174–181.
- Knorr, D., Pelloux, R. M. (1982), *Met. Trans.* 13 A, 73–83.
- Konashi, K. (1984), *J. Nucl. Mater.* 125, 244–247.
- Kubo, T., Wakashima, Y., Imahashi, H., Nagai (1985), *J. Nucl. Mater.* 132, 126–136.
- Lemaignan, C. (1992), *J. Nucl. Mater.* 187, 122–130.
- Levy, S. (1974), *Nucl. Eng. & Design* 29, 157–162.
- Lloyd, L. T. (1963), *ANL 6591*.
- Lucas, G., Pelloux, R. M. (1981), *Nucl. Tech.* 53, 46–57.
- Lukas, S. R. (1988), *J. Nucl. Mater.* 158, 240–252.
- Lustman, B., Kerze, F. (1955), *The Metallurgy of Zr*. New York: McGraw-Hill.
- MacEwen, S. R., Faber, J. Jr., Turner, A. L. P. (1983), *Acta Metall.* 5, 657–676.
- MacEwen, S. R., Christodoulou, N., Tome, C., Jackman, J., Holden, T. M., Faber, J. Jr., Hitterman, R. L. (1988), *8th Int. Conf. Text. Mat. (ICTOM 8): Kallend, J. S., Gottstein, G. (Eds.)*. Warrandale, PA: Met. Soc. pp. 825–836.
- Marlowe, M. O., Armijo, J. S., Cheng, B., Adamson, R. (1985), *Proc. ANS Top. Meet. Light Water Reactor Performance, April 21–24, Orlando, FL*. La Grange Park, IL: ANS, pp. 3–73, 3–90.
- Matsuo, Y. (1987), *J. Nucl. Sci. Tech.* 24, 111–119.
- Matsuo, Y. (1989), *8th Int. Conf. Zr Nucl. Ind., June 19–23, 1988, San Diego, CA: ASTM-STP 1023*. Philadelphia, PA: Am. Soc. Test. Mat., pp. 678–691.
- Matthews, J. R., Finnis, M. W. (1988), *J. Nucl. Mater.* 159, 257–285.
- McInteer, W. A., Baty, D. L., Stein, K. O. (1989), *8th Int. Conf. Zr Nucl. Ind., June 19–23, 1988, San Diego, CA: ASTM-STP 1023*. Philadelphia, PA: Am. Soc. Test. Mat., pp. 621–640.
- Miquet, A., Charquet, D., Michaut, C., Allibert, C. H. (1982), *J. Nucl. Mater.* 105, 142–148.
- Morize, P. (1984), *Ann. Chim. Fr.* 9, 411–421.
- Motta, A. T., Lemaignan, C. (1992), in: *Ordering and Disorder in Alloys: Yavari, A. R. (Ed.)*. London: Elsevier Applied Science, pp. 255–275.
- Motta, A. T., Olander, D. R., Machiels, A. J. (1989), *14th ASTM Int. Symp. Effects Irradiation Mater., ASTM STP 1046*. Philadelphia, PA: Am. Soc. Test. Mat., pp. 457–469.

- Motta, A. T., Olander, D. R. (1990), *Acta Metall. Mater.* 38(11), 2175–2185.
- Motta, A. T., Lefebvre, F., Lemaignan, C. (1991), *9th Int. Symp. Zr Nucl. Ind., Nov. 1990, Kobe, Japan: ASTM-STP 1132*. Philadelphia, PA: Am. Soc. Test. Mat., pp. 718–739.
- Motta, A. T., Lemaignan, C., Olander, D. R. (1992), *15th ASTM Int. Symp. Effects Irradiation Mater., Nashville 1990, ASTM STP 1125*. Philadelphia, PA: Am. Soc. Test. Mat., pp. 689–702.
- Moulin, L., Reschke, S., Tenckhoff, E. (1984a), *6th Int. Conf. Zr Nucl. Ind., June 28–July 1, 1982, Vancouver, Canada: ASTM-STP 824*. Philadelphia, PA: Am. Soc. Test. Mat., pp. 225–243.
- Moulin, L., Thouvenin, J.P., Brun, P. (1984b), *6th Int. Conf. Zr Nucl. Ind., June 28–July 1, 1982, Vancouver, Canada: ASTM-STP 824*. Philadelphia, PA: Am. Soc. Test. Mat., pp. 37–44.
- Murthy, K. L., Adams, B. L. (1985), *Mater. Sci. Eng.* 70, 169–180.
- Nash, P., Jayanth, C. S. (1984), *Bull. Alloy Phase Diagrams* 5(2), 1777–1779.
- Nikulina, A. V., Markelov, V. A., Peregud, M. M., Voevodin, V. N., Panchenko, V. L., Kobylansky, G. P. (1993), *3rd Int. Conf. Evolution of Microstructure in Metals During Irradiation, Muskoka, Canada, Sept.–Oct. 1992*, to be published in the *J. Nucl. Mater.*
- Northwood, D. O., Gilbert, R. W., Bahlen, L. E., Kelly, P. M., Blake, R. G., Jostsons, A., Madden, P. K., Faulkner, D., Bell, W., Adamson, R. B. (1979), *J. Nucl. Mater.* 79, 379–394.
- Olander, D. R. (1976), *Fundamental Aspects of Nuclear Reactor Fuel Elements, TID-26711-P1*. Springfield, VA: National Technical Information Service.
- Parsons, J. R., Hoelke, C. W. (1989), *14th ASTM Int. Symp. Effect Irradiation Mater., ASTM STP 1046*. Philadelphia, PA: Am. Soc. Test. Mat., pp. 689–702.
- Pêcheur, D., Lefebvre, F., Motta, A. T., Lemaignan, C., Wadier, J. F. (1992), *J. Nucl. Mater.* 189, 318–332.
- Peehs, M., Stehle, H., Steinberg, E. (1979), *4th Int. Conf. Zr Nucl. Ind.: ASTM-STP 681*. Philadelphia, PA: Am. Soc. Test. Mat., pp. 244–260.
- Ploc, R. A. (1983), *J. Nucl. Mater.* 113, 75–80.
- Porrot, E., Eminet, G., Baudusseau, C., Lemaignan, C. (1991), *IAEA Tech. Com. Meet. Post Irrad. Eval. Techn. Reactor Fuel, Sept. 11–14, 1990, Workington, England: IWGFPT/37*, pp. 77–82.
- Price, E. G., Richinson, P. J. (1978), *AECL 6345*.
- Ramasubramanian, N. (1989), *Proc. Tech. Com. Meet. IAEA: Fundamental Aspects of Corrosion in Zr Base Alloys in Water Reactors Environments, Sept. 11–15, Portland, OR: IWGFPT/34*, pp. 36–44.
- Ramasubramanian, N. (1991), *9th Int. Conf. Zr Nucl. Ind., Nov. 1990, Kobe, Japan: ASTM-STP 1132*. Philadelphia, PA: Am. Soc. Test. Mat., pp. 613–623.
- Rogerson, A. (1988), *J. Nucl. Mater.* 159, 43–61.
- Rosenbaum, H., Lewis, J. E. (1977), *J. Nucl. Mater.* 67, 237–282.
- Rosenbaum, H., Davis, J. H., Pon, J. Q. (1966), *GEAP 5100-5*.
- Rosenbaum, H., Rand, R. A., Tucker, R. P., Cheng, B., Adamson, R. B., Davies, J. H., Armijo, J. S., Wiesner, S. B. (1987), *7th Int. Conf. Zr Nucl. Ind.: ASTM-STP 939*. Philadelphia, PA: Am. Soc. Test. Mat., pp. 675–699.
- Sayers, C. M. (1987), *J. Nucl. Mater.* 144, 211–213.
- Schemel, J. H. (1977), *ASTM Manual on Zirconium and Hafnium: ASTM-STP 639*. Philadelphia, PA: Am. Soc. Test. Mat.
- Schemel, J. H. (1987), *7th Int. Conf. Zr Nucl. Ind. ASTM-STP 939*. Philadelphia, PA: Am. Soc. Test. Mat., pp. 243–256.
- Schuster, I., Lemaignan, C. (1992), *J. Nucl. Mater.* 189, 157–166.
- Shaltiel, D., Jacob, I., Davidov, D. (1976), *J. Less. Comm. Met.* 53, 117–131.
- Simpson, L. A., Chow, C. K. (1987), *7th Int. Conf. Zr Nucl. Ind.: ASTM-STP 939*. Philadelphia, PA: Am. Soc. Test. Mat., pp. 579–596.
- Smith, T. (1969), *J. Electrochem. Soc.* 112, 560–567.
- Stephen, W. W. (1984), *6th Int. Conf. Zr Nucl. Ind., June 28–July 1, 1982, Vancouver, Canada. ASTM-STP 824*. Philadelphia, PA: Am. Soc. Test. Mat., pp. 5–36.
- Tenckhoff, E. (1978), *Met. Trans.* 9A, 1401–1412.
- Tenckhoff, E. (1988), *Deformation Mechanisms, Texture and Anisotropy in Zirconium and Zircalloys ASTM-STP 966*. Philadelphia, PA: Am. Soc. Test. Mat.
- Tricot, R. (1989), *Matériaux et Techniques, Avril–Mai*, 1–32.
- Tricot, R. (1990), *Rev. Gén. Nucl. Jan.–Fév.*, 8–20.
- Urbanc, V. F., Warr, B. D., Manolescu, A., Chow, C. K., Shanahan, M. W. (1989), *8th Int. Conf. Zr Nucl. Ind., San Diego, CA, June 1988, ASTM STP 1023*, 20–34.
- Wadekar, S., Banerjee, S., Raman, V. V., Asundi, M. K. (1991), *9th Int. Conf. Zr Nucl. Ind., Nov. 1990, Kobe, Japan: ASTM-STP 1132*. Philadelphia, PA: Am. Soc. Test. Mat., pp. 140–155.
- Warr, B. D., Elmoselhi, M. B., Brennenstuhl, A., Lichtenberger, P. C., Newcomb, S. B., McIntyre, N. S. (1991), *9th Int. Conf. Zr Nucl. Ind., Nov. 1990, Kobe, Japan. ASTM-STP 1132*. Philadelphia, PA: Am. Soc. Test. Mat., pp. 740–757.
- Weatherly, G. C. (1981), *Acta Metall.* 29, 501–512.
- Wiedersich, H. (1972), *Rad. Effects* 12, 111–125.
- Williams, C. D., Gilbert, R. W. (1966), *J. Nucl. Mater.* 18, 161–166.
- Woo, C. H. (1979), *ASTM-STP 683*. Philadelphia, PA: Am. Soc. Test. Mat., pp. 640–655.
- Woo, C. H. (1984), *J. Nucl. Mater.* 120, pp. 55 ff.
- Woo, C. H. (1988), *J. Nucl. Mater.* 159, 237–256.
- Woo, C. H., Singh, B. N. (1992), *Phil. Mag. A* 65, 889–912.

- Woo, C. H., Causey, A. R., Holt, R. A. (1990), invited paper in: *Diffusion and Defect Solid State Data*, in press.
- Woo, C. H., Holt, R. A., Griffiths, M. (1992), in: *Materials Modeling from theory to Technology*. Bristol: Institute of Physics Publications, pp. 55–60.
- Woo, O. T., Carpenter, G. J. C. (1987), *J. Nucl. Mater.* 159, 397–404.
- Wood, J. C., Kelm, J. R. (1980), *IAEA Spec. Meet on: Pellet Cladding Interaction in Water Reactors, Risø, Denmark. IWGFPT/8*.
- Yang, W. J. S. (1989), *14th Int. Symp. Effects Rad. Mater., 1988 Andover, MA: ASTM-STP 1046*. Philadelphia, PA: Am. Soc. Test. Mat., pp. 442–456.
- Yang, W. J. S., Tucker, R. P., Cheng, B., Adamson, R. B. (1986), *J. Nucl. Mater.* 138, 185–195.
- Zee, R. H., Rogerson, A., Carpenter, G. J. C., Waters, J. (1984), *J. Nucl. Mater.* 120, 223–229.
- Zhou, H. (1992), Chalk River, unpublished results.
- Zuzek, E., Abriata, J. P., San Martin, A., Manchester, F. D. (1990), *Bull. Alloy Phase Diagrams* 11(4), 385–395.

General Reading

- ASTM-STP* series of conferences on Zr in the nuclear industry nos. 1 to 9. Philadelphia, PA. Am. Soc. Test. Mat.
- Cheadle, B. A. (1975), *The Physical Metallurgy of Zr Alloys, CNRL Report*, 1208.
- Conferences on microstructural evolution under irradiation: *Journal of Nuclear Materials* 90 (1980) and 159 (1988).
- Douglass, D. L. (1971), *The Metallurgy of Zirconium, Atomic Energy Review*, Vienna.
- Tenckhoff, E. (1978), *Met. Trans.* 9A, 1401–1412.